



UNIVERSITY OF COPENHAGEN  
FACULTY OF SCIENCE

---

# Master's Thesis

## Observations of Turbulent Dynamics in the Baltic Sea

Olga Lia Dimopoulou  
zpv515@alumni.ku.dk

Supervisor: Markus Jochum  
Co-Supervisor: Lars Umlauf

January 4, 2019



# Abstract

Some of the most important mixing processes of the Baltic Sea are investigated here using high-resolution velocity and turbulence measurements obtained during a mid-autumn research cruise (2017) in the Eastern Gotland Basin. First, the dynamics of near-inertial waves and their relation to mixing are studied. In the absence of tides, the basin-scale energetics are found to be dominated by near-inertial motions. These motions generate enhanced shear layers which could be associated with bands of elevated dissipation rates of turbulent kinetic energy observed within and below the halocline. Then, the focus is narrowed to the surface boundary layer. Traditionally, the surface boundary layer is believed to be driven by the atmosphere through fluxes of heat, momentum and moisture. However, observations presented here suggest that lateral density gradients and their geostrophic currents may also play a role in the surface boundary layer dynamics.



# Acknowledgments

I would like to thank my supervisor, Markus Jochum, for inspiring me to step into the world of Physical Oceanography. I would also like to thank my co-supervisor, Lars Umlauf, for having me on the cruise and for the help he offered over the past year. I would like to express my gratitude to my family and friends for their moral support and for proofreading my work. A special thanks, however, goes to my friend Euphrates who taught me how to use MATLAB and has encouraged me throughout my years in Physics. Last but not least, I would like to thank the crew of R/V Elisabeth Mann Borgese.

This thesis is a contribution to project T2 (Energy budget of the ocean surface mixed layer) of the Collaborative Research Center TRR 181 “Energy Transfer in Atmosphere and Ocean”, funded by the German Research Foundation under grant 274762653. Partial support from this project is appreciated.

# Contents

<b>1</b>	<b>Introduction</b>	<b>1</b>
<b>2</b>	<b>The Baltic Sea</b>	<b>3</b>
2.1	The Baltic Sea . . . . .	3
2.2	Mixing Processes in the Baltic Proper . . . . .	6
<b>3</b>	<b>Theoretical Background</b>	<b>9</b>
3.1	Turbulence and mixing . . . . .	9
3.1.1	Turbulent Kinetic Energy Equation . . . . .	11
3.2	Internal Gravity Waves . . . . .	14
3.2.1	Near-Inertial Waves . . . . .	17
3.3	Lateral Variability in the Surface Boundary Layer . . . . .	17
<b>4</b>	<b>Study Area and Measurements</b>	<b>21</b>
4.1	Study Area . . . . .	21
4.2	Moored Measurements . . . . .	22
4.2.1	Acoustic Doppler Current Profilers . . . . .	23
4.3	Ship-Based Measurements . . . . .	24
4.3.1	Microstructure Measurements . . . . .	24
4.3.2	Meteorological data . . . . .	26
<b>5</b>	<b>Observations</b>	<b>29</b>
5.1	Current Structure in the Eastern Gotland Basin . . . . .	29
5.1.1	Near- $f$ Wave Motions . . . . .	30
5.2	Dissipation Measurements . . . . .	35
5.2.1	Stratification Parameters . . . . .	35
5.2.2	Mixing Parameters . . . . .	37
5.3	Turbulence in the Surface Boundary Layer . . . . .	40
<b>6</b>	<b>Summary</b>	<b>43</b>
6.1	Summary . . . . .	43
6.2	Future Work . . . . .	44
<b>A</b>	<b>Derivation of the Internal Gravity Wave Equation</b>	<b>45</b>

**B Digital Filters**

**47**

**Bibliography**

**51**

# Chapter 1

## Introduction

Physical processes in the ocean span a wide range of spatial and temporal scales. Atmospheric buoyancy forcing, winds and tides are processes that occur over horizontal scales of  $\mathcal{O}(100-1000)$  km, driving basin scale gyres, the meridional overturning circulation and wave motions such as Rossby, Kelvin and internal waves. A range of dynamical processes ultimately lead to viscous dissipation at small scales, at the boundaries as well as in the interior of the ocean. Turbulent mixing processes in the ocean play a primary role in the dynamics of marine ecosystems; knowledge of turbulence and its effects is crucial in understanding how the ocean works.

Ocean turbulence ranges from the basin scale down to the scale of molecular viscosity. It is inherently unsteady and chaotic, therefore, observing it is rather a challenging task. Moreover, the ocean's vast size and its unpredictable and constantly changing forcings, introduce further complexities. Microstructure measurements in the ocean, measurements on small spatial scales of  $\mathcal{O}(1)$  cm, are relatively recent with the first observations taking place in the 1950's (Stewart and Grant, 1962). These measurements resolve the Kolmogorov scale, the scale at which turbulent kinetic energy is dissipated into heat.

The Baltic Sea is considered an ideal laboratory for studying mixing processes without the influence of tides; its character as an almost enclosed marginal sea strongly damps the tidal signal (Reissmann et al., 2009). Among the several mechanisms that support turbulent mixing in the Baltic Sea, the physical processes that are central in this thesis are internal gravity waves and lateral density fronts. First, the interest lies in the direct measurements of the dissipation of turbulent kinetic energy in the Eastern Gotland Basin, and in the association of these estimates to the wind and parameters of the internal wave field. The description of the temporal and spatial variability in velocity, temperature and salinity provides an important framework for interpreting measurements of the turbulent energy dissipation rate. Afterwards, the focus is constrained on the surface boundary layer, where lateral density gradients and their impact on surface layer mixing are discussed.

The manuscript is organized as follows: after this brief introduction, the bathymetry and hydrography of the Baltic Sea followed by some of the its most important mixing processes, are described in Chapter 2. In Chapter 3, one will find a theoretical background in turbulence and a discussion about internal gravity waves and lateral density gradients, es-

essential for the understanding of the main part of this thesis. A description of the study area and instruments used during the cruise is provided in Chapter 4. Chapter 5 is dedicated to the analysis of the obtained measurements. First observations of near-inertial waves are discussed, followed by observations of lateral density gradients. Finally, a summary and some ideas for future work provided in Chapter 6, complete the thesis.

# Chapter 2

## The Baltic Sea

### 2.1 The Baltic Sea

The Baltic Sea is a semi-enclosed sea with very weak tidal motion, located in northern Europe from 54°N to 66°N and from 10°E to 30°E. More than one third of the Baltic Sea is shallower than 30 m, giving it a small total volume ( $21.5 \times 10^3 \text{ km}^3$ ) compared to its surface area ( $4.2 \times 10^5 \text{ km}^2$ ) (HELCOM, 2002). Based on its topographical formations, the Baltic Sea is geographically divided into several basins connected by channels and separated by sills (Fig. 2.1). In its outermost part, starting from the west, lies the Kattegat, which constitutes the transition zone between the Baltic Sea and the North Sea. South of the Kattegat follow three narrow straits, the Little Belt, the Great Belt and the Øresund, also known as the Danish Straits. To the south of the Øresund is the 7 m deep Drogden Sill, while to the south of the Belt Sea, is the Fehmarn Belt followed by the 18 m deep Drass Sill. East of the Sills is the first main basin of the Baltic Sea, the Arkona Basin, located between Sweden and Germany. The Arkona Basin has a maximum depth of 45 m and is connected to the Bornholm Basin through the Bornholm Channel. The Bornholm Basin, located between Sweden and Poland, has a maximum depth of, approximately, 100 m. East of the Bornholm Basin, over the 60 m deep Slupsk Sill and through the Slupsk Furrow, lies the Gdansk Basin with a maximum depth of 110 m. In the northeast direction, the Slupsk Furrow is connected to the Eastern and Western Gotland Basins. The Eastern Gotland Basin is the largest and the most central basin of the Baltic Sea and has a maximum depth of 259 m. On the other hand, the Western Gotland Basin, which is located southeast of Stockholm, contains the deepest point of the Baltic Sea, the Landsort Deep (459 m). The Gotland Sea, which includes the Western and Eastern Gotland Basins and the Gdansk Basin, contains half of the Baltic Sea's water mass. East and north of the Gotland Sea lie three major gulfs, the Gulf of Riga, the Gulf of Finland and the Gulf of Bothnia. The Gulf of Riga is surrounded by Estonia and Latvia, the Gulf of Finland by Estonia, Finland and Russia and the Gulf of Bothnia by Finland and Sweden. The latter is the northernmost part of the Baltic Sea and consists of the following basins: the Åland Sea, the Bothnian Sea and the Bay of Bothnia (Leppäranta and Myrberg, 2009). About 70% of river runoff enters

these Gulfs, representing the prime source of freshwater in the Baltic Sea (Bergström and Carlsson, 1994) and regulating the salinity of the Baltic surface water.

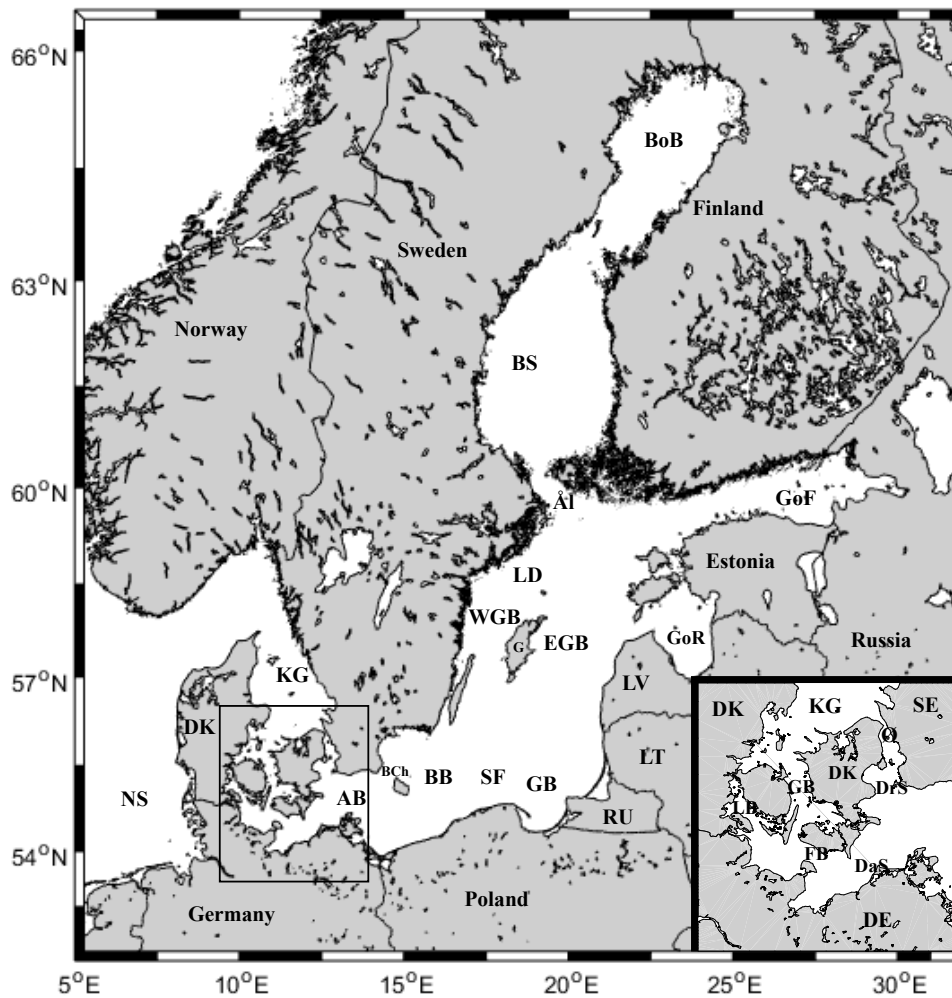


Figure 2.1: Map of the Baltic Sea. Indicated regions are the North Sea (NS), the Kattegat (K), the Øresund (Øs), the Great Belt (GB), the Little Belt (LB), the Fehmarn Belt (FB), the Drogden Sill (DrS), the Darss Sill (DaS), the Arkona Basin (AB), the Bornholm Channel (BCh), the Bornholm Basin (BB), the Slupsk Furrow (SF), the Gdansk Basin (GB), Gotland (G), the Eastern Gotland Basin (EGB), the Western Gotland Basin (WGB), the Landsort Deep (LD), the Gulf of Riga (GoR), the Gulf of Finland (GoF), the Åland Sea (Å), the Bothnian Sea (BS) and the Bay of Bothnia (BoB). Indicated countries are Denmark (DK), Russia (RU), Lithuania (LT), Latvia (LV), Sweden (SE), Germany (DE).

Compared to the open ocean and the North Sea, the salinity of the Baltic Sea is generally low and its water mass is brackish. Precipitation ( $237 \text{ km}^3/\text{y}$ ) and river runoff ( $428 \text{ km}^3/\text{y}$ ) exceed evaporation ( $184 \text{ km}^3/\text{y}$ ) leading to a mean annual freshwater surplus of  $481 \text{ km}^3$  (Feistel et al., 2008). As the density of the freshwater is lower than that of the marine water, it remains at the surface layer. Therefore, surface salinities vary from a maximum of  $25 \text{ g/kg}$  in the transition area of the Kattegat to a minimum of about  $5 \text{ g/kg}$  in the Gulf of Bothnia, with intermediate values of over  $9 \text{ g/kg}$  in the Arkona Basin and  $7 \text{ g/kg}$  in the Gotland Basin (Reissmann et al., 2009). Moreover, the high net freshwater supply creates a slight elevation of the central Baltic Sea mean sea level compared to the mean sea level of the Kattegat, leading to a pressure gradient. This pressure gradient drives a barotropic outflow of brackish surface water through the Danish Straits and the Kattegat into the North Sea. The outflow of brackish surface waters is compensated by a near bottom inflow of saltier waters from the North Sea. However, such inflows are restricted by the narrow channels and shallow sills and the permanently changing wind conditions. Only major episodic inflows caused by specific meteorological and oceanographic circumstances, can transport substantial amounts of saline and oxygenated water into the inner Baltic Sea, renewing the central Baltic deep water. These major inflows are often classified into barotropic and baroclinic (Reissmann et al., 2009):

- Barotropic inflows, also known as the Major Baltic Inflows, are forced by barotropic pressure gradients, i.e. sea level differences. They appear during persistent westerly winds only when prior long lasting easterly winds, of the order of two weeks, have lowered the sea level of the Baltic Proper by  $10 \text{ cm}$  relative to the Danish Straits and the Kattegat (Matthäus and Franck, 1992; Reissmann et al., 2009). These types of inflows occur mostly in late autumn, winter and early spring, on decadal timescales (Matthäus and Franck, 1992) due to the specific meteorological conditions required.
- Baroclinic inflows, on the other hand, are driven by baroclinic pressure gradients caused by lateral salinity differences across the Danish Straits. They usually appear in late summer, under long lasting calm wind conditions (Feistel et al., 2008) and they are much weaker compared to the barotropic inflow events. Nonetheless, they can transport substantial amounts of warm and saline water across the Darss Sill, into the intermediate layers of the central Baltic Sea.

The large river discharge and the inflows of saline ocean waters, combined with solar radiation and heat exchange with the atmosphere, are responsible for the formation of a complex and variable thermohaline stratification throughout the Baltic Sea. The upper and intermediate layers are separated by a thermocline and the intermediate and deep layers by a halocline. The strong and permanent halocline coincides with the pycnocline which limits the vertical range of wind mixing and convection (Matthäus and Franck, 1992; Rak and Wiczorek, 2012). The depth of the halocline depends on the depth of the basin and can become shallower after strong inflow events. Deepening from southwest to northeast, the halocline is located at about  $40 \text{ m}$  depth in the Arkona Basin, at  $50 \text{ m}$  depth in the Bornholm Basin, at  $60 \text{ m}$  depth in the Gdansk Basin and at  $70$  to  $90 \text{ m}$  in the

Eastern Gotland Basin (Reissmann et al., 2009; Rak and Wieczorek, 2012). During spring, a seasonal thermocline develops in the upper 20 to 30 m of the water column, separating the warm upper layer from the cold intermediate water, which disappears during fall due to cooling and mixing of the surface water by wind and convection. However, these processes do not affect the deep waters which are isolated from the surface waters by the halocline

To conclude, the Baltic Sea exhibits a complex overturning circulation in which the outflow of brackish surface water is balanced by irregular inflow events of saline water, and the circulation is closed by upwelling and diapycnal mixing processes. However, the circulation in the Baltic Sea is limited, because it is restricted in the horizontal by bottom topography and in the vertical by the permanent halocline (Matthäus and Franck, 1992).

## 2.2 Mixing Processes in the Baltic Proper

Vertical mixing and transport processes are important to understand the overturning circulation of the Baltic Sea. Therefore, some of the most important mixing processes of the Baltic Proper, the area of the Baltic Sea which contains the Bornholm and the Gotland Basins, are briefly presented below.

- **Bottom gravity currents.** Episodic inflows over the Belt Sea sills transport saline North Sea water into the entrance areas of the Baltic Sea. Depending on their volume and their density, these inflows form dense bottom gravity currents which supply the bottom waters of the Arkona Basin, the Bornholm Basin and the Gotland Basin with salt and oxygen (Reissmann et al., 2009). The effect of the bottom gravity currents decreases along their way to the central Baltic due to mixing with the less saline and hence, less dense ambient water (Köuts and Omstedt, 1993). Once the density of the inflowing waters equals that of the surrounding waters, they interleave with the ambient water masses to their equilibrium depth. Through this mechanism, the Baltic Sea deep waters are ventilated on decadal time scales.
- **Inertial waves and internal wave breaking.** Turbulence below the surface mixed layer is independent of the wind forcing and occurs as intermittent patches which is related to pelagic and benthic decay of internal waves (Lass et al., 2003). Non-linear interactions of internal waves, cascade energy from the large energy containing waves towards the small scale waves that become unstable and finally break into turbulent motion. A study in the interior of the Bornholm Basin by Van der Lee and Umlauf (2011), showed a clear correlation between narrow near-inertial shear bands and increased mixing rates, identifying shear from near-inertial waves to be the primary source of mixing.
- **Boundary mixing processes.** Boundary mixing encapsulates several mixing processes at the boundary, such as breaking of internal waves or collapse of mesoscale eddies on the topography. According to the no-slip condition, bottom friction forces

the current velocities to decrease towards the boundary until they reach zero velocities at the boundary. Subsequently, the resulting shear causes turbulence. The relevance of boundary mixing in the Baltic Sea was studied by [Holtermann et al. \(2012\)](#) who observed the spreading of a passive tracer which was injected below the halocline and above the bottom boundary layer in the center of the Eastern Gotland Basin during the Baltic Sea Tracer Release Experiment. The authors found that the vertical mixing rates were substantially increased after the tracer had reached the lateral boundaries of the basin, concluding that boundary mixing is a crucial component of basin scale vertical mixing.

- **Mesoscale eddies.** Mesoscale eddies, or the so called Beddies in case of the Baltic Sea eddies, are vortices with a horizontal scale of  $\mathcal{O}(10-100)$  km. They transport energy and momentum and may contain different water properties than their surroundings ([Reissmann et al., 2009](#)). They contribute to diapycnal mixing through two mechanisms: firstly, through vertical displacement of isopycnals caused by their rotation and geostrophic adjustment, and secondly through their decay process or collapse during which they release the stored potential and kinetic energy. The released energy is available for turbulence and thus, diapycnal mixing, and also for internal wave radiation ([Reissmann et al., 2009](#)).
- **Fronts.** Fronts are regions with large horizontal density gradients and are common features in the Baltic Sea. They can be as narrow as hundreds of meters and as wide as tens of kilometers. The convergence of waters at an ocean front results to their rapid sink, with vertical velocities of 10 to 100 m d<sup>-1</sup>, compared to typical rates of 1 to 10 m d<sup>-1</sup> in the rest of the ocean. Thus, fronts are important features in the oceans as they enhance the vertical transport of tracers such as heat and nutrients ([Ferrari, 2011](#)).

Among the physical processes mentioned above, mixing related to internal waves and fronts are mainly in the focus of this thesis and are, therefore, discussed in further detail in the following chapter.



# Chapter 3

## Theoretical Background

### 3.1 Turbulence and mixing

Turbulence is an energetic, rotational and eddying state of motion that results in the transport of matter, heat, and momentum at much higher rates than those of molecular processes alone (Thorpe, 2005). One of the most important properties of turbulence is that, by generating relatively large velocity gradients at small scales, typically 1 mm to 1 cm, it is dissipative with kinetic energy transferred into heat due to viscous friction. Turbulence, therefore, requires a continuous supply of energy from an external source, such as the atmosphere or through the tide-generating gravitational forces of the Moon and Sun, to compensate for the viscous losses. In 1883, Osborne Reynolds, one of the pioneers in the scientific study of turbulence, showed how a smooth flow of water through a long circular tube becomes turbulent when the mean speed of the flow,  $U$ , exceeds a value that is related to the diameter of the tube,  $d$ , and to the kinematic viscosity of the water,  $\nu$ . In his laboratory experiments, Reynolds injected a streak of ink into the water entering one end of a horizontal tube, with a diameter varying between 0.6 to 2.5 cm, from a large tank of stationary water. He observed that when the velocities were sufficiently low, the streak of color extended in a straight line through the tube without much mixing taking place between the ink and the surrounding water (Fig. 3.1a). As the velocities increased, the streak of color developed eddies at a considerable distance from the intake which mixed the ink over the full diameter of the tube, clearly showing the strong relation between turbulence and mixing (Fig. 3.1c). He concluded that the laminar flow turns into a random eddying turbulent motion when a non-dimensional quantity, known as the Reynolds number,

$$Re = \frac{Ud}{\nu}, \quad (3.1)$$

exceeds a value of about  $1.3 \times 10^4$ , where  $\nu$  is approximately  $10^{-6} \text{ m}^2 \text{ s}^{-1}$  for water. In the ocean, the values of  $U$  and  $d$  appearing in Eq. 3.1 are usually regarded as those characterizing the flow, for example, the mean speed of the local flow and water depth. The characteristic  $Re$  in the ocean commonly exceeds a value of  $10^4$ .

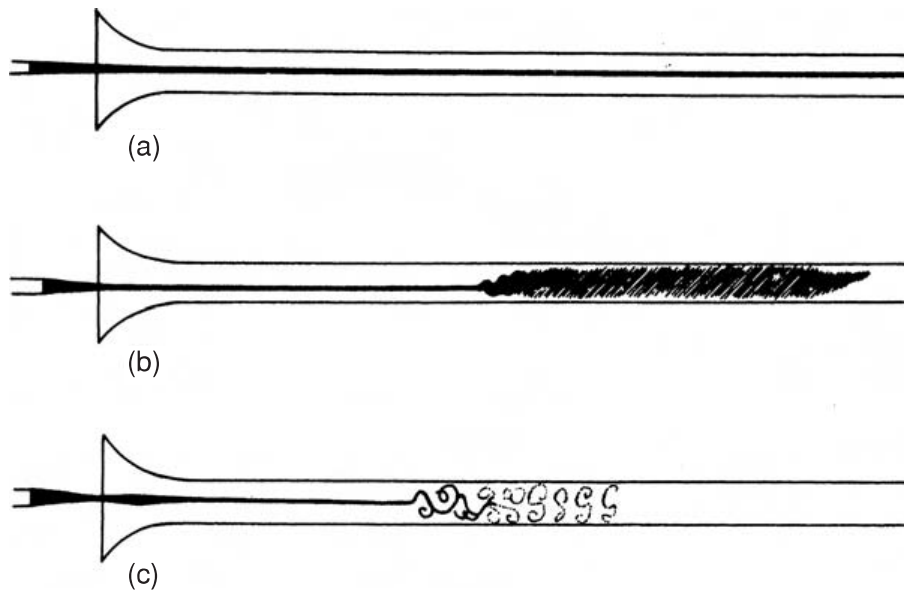


Figure 3.1: Osborne Reynolds' experiment. Appearance of streak of ink in water flowing from left to right through a glass tube (a) Laminar flow (or steady flow) at sub-critical Reynolds number. (b) Turbulent flow at super-critical Reynolds number. (c) Turbulent flow when the ink is illuminated by a spark. Notice how the illustrated eddies are of size comparable to the diameter of the tube,  $d$ . (Figure adapted from [Reynolds \(1883\)](#))

Turbulent mixing can be viewed as a two-stage process as described by [Eckart \(1948\)](#), that of stirring and mixing. During the stirring phase, shear <sup>1</sup> and strain <sup>2</sup> produced by turbulent motions promote narrow filamentary distributions of water properties, like those observed when cream is stirred into a cup of coffee or the eddies observed in Reynolds' experiment (Fig. 3.1c). Fluid particles, initially close together, become separated or dispersed by turbulence; the stirring extends the surfaces of contact between fluid volumes, increasing the areas across which diffusive transfers of fluid properties, such as temperature, may occur. This process increases gradients to such an extent, that a second process comes into play, that of mixing, where molecular diffusion causes transfers of fluid properties that rapidly reduce the gradients and the extremes of temperature or solute concentration. Thus, the action of turbulence is one of dispersion of material particles by stirring whilst homogenizing, or mixing, fluid properties and it is irreversible. A visualization of this can be seen in the famous chessboard figure by [Welander \(1955\)](#), adapted here in Fig. 3.2.

<sup>1</sup> Shear is the spatial gradient of the speed of a current in a direction normal to the flow.

<sup>2</sup> Strain in stratified fluids is defined as the vertical distance between two isopycnals divided by their mean distance. Strain is positive when isopycnals are further apart than on average.

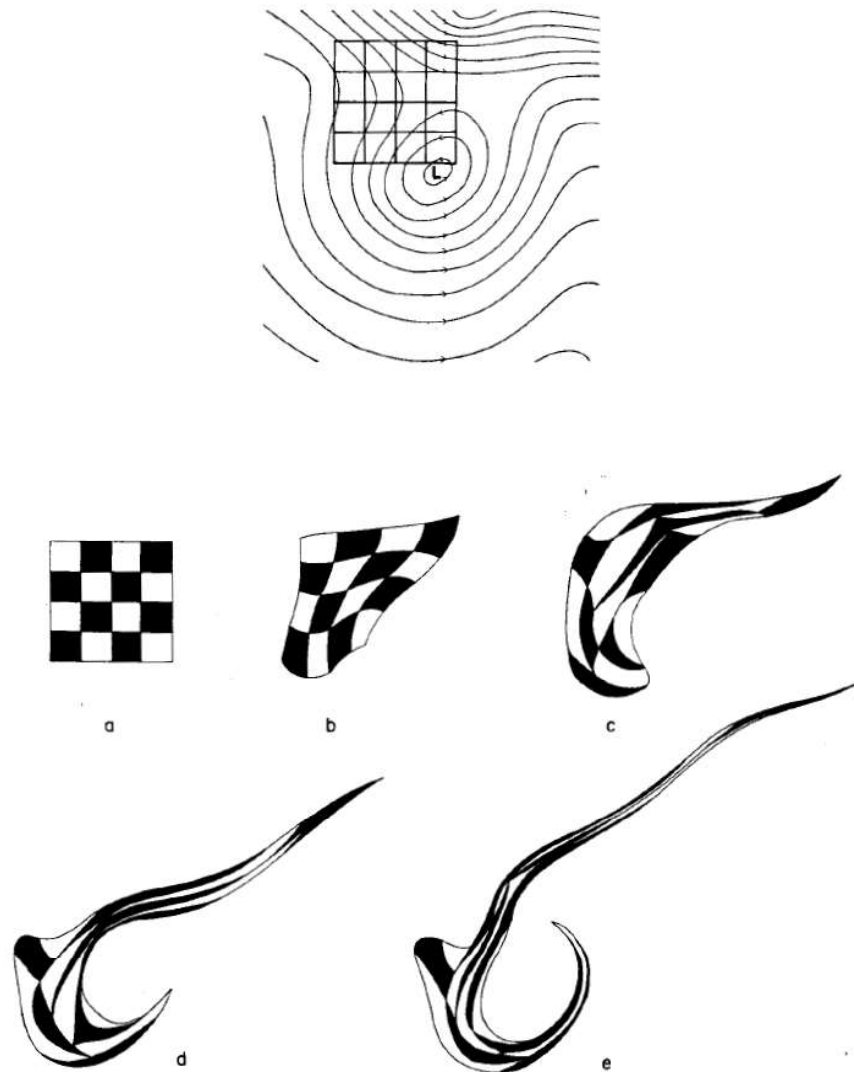


Figure 3.2: Stirring without mixing of a passive tracer. The initial streamlines of the 2-D turbulent flow are shown on top. The flow deforms the chessboard pattern into elongated filaments. (Figure adapted from [Welander \(1955\)](#))

### 3.1.1 Turbulent Kinetic Energy Equation

Turbulent flows satisfy the Navier-Stokes equations of motion. However, the scales of turbulent flows in the ocean range between hundreds of kilometers (in our case the size of the Gotland Basin) down to the order of millimeters. This means that it is impossible to predict the flow in detail due to the enormous range of scales that need to be resolved. Nevertheless, it is neither feasible nor desirable to consider in detail all of the small-scale fluctuations, and the interest is in the mean characteristics, such as the distribution of mean velocity and temperature. The evolution of the averaged quantities can be calculated by

decomposing each quantity into a mean (indicated by angle brackets) and into a fluctuating component (denoted by apostrophe), an approach known as Reynolds decomposition, such that, for a quantity  $a$ :

$$a = \langle a \rangle + a'. \quad (3.2)$$

Some of the properties of the decomposed quantities are the following: i) the average of the fluctuating component of a variable,  $a$ , is zero,  $\langle a' \rangle = 0$ , ii) the average of the sum of two variables,  $a_1$  and  $a_2$ , is equal to the sum of the average of each variable,  $\langle a_1 + a_2 \rangle = \langle a_1 \rangle + \langle a_2 \rangle$ , iii) averaging an already averaged variable has no effect,  $\langle \langle a \rangle \rangle = \langle a \rangle$ , and iv) the average of a fluctuating component of a quantity times the average component of the same quantity is equal to zero,  $\langle a' \langle a \rangle \rangle = 0$ .

To derive the turbulent kinetic energy equation (TKE), the starting point is the Navier-Stokes equations of motion. Therefore, the equations of motion in the Boussinesq approximation, for a non-rotating frame and in Einstein notation, are of the form:

$$\frac{\partial u_i}{\partial t} + u_j \frac{\partial u_i}{\partial x_j} = -\frac{1}{\rho_0} \frac{\partial p}{\partial x_i} + \frac{\rho}{\rho_0} g_i + \frac{\partial}{\partial x_j} \left( \nu \frac{\partial u_i}{\partial x_j} \right), \quad (3.3)$$

$$\frac{\partial u_i}{\partial x_i} = 0, \quad (3.4)$$

where  $u_1 = u$ ,  $u_2 = v$ ,  $u_3 = w$  are the velocities in the  $x_1 = x$  (eastward),  $x_2 = y$  (northward) and  $x_3 = z$  (upward) directions, respectively,  $t$  represents time,  $\rho$  density,  $\rho_0$  a constant reference density,  $p$  pressure and  $\vec{g} = (0, 0, -g)$  is the gravity vector. Furthermore,  $\nu$  is the kinematic viscosity for water which varies with temperature such that at 10 °C,  $\nu = 1.3 \times 10^{-6} \text{ m}^2 \text{ s}^{-1}$  and at 30 °C, it decreases to  $\nu = 8 \times 10^{-7} \text{ m}^2 \text{ s}^{-1}$ . The incompressibility condition (Eq. 3.4) results from the Boussinesq assumption in which density is assumed to be constant everywhere, except in the buoyancy frequency term on the right hand side.

The variables of the above equations can be decomposed into their mean part and a deviation from the mean according to Reynolds decomposition (Eq. 3.2), such that:

$$\begin{aligned} u_i &= \langle u_i \rangle + u'_i, \\ p &= \langle p \rangle + p', \\ \rho &= \langle \rho \rangle + \rho', \end{aligned} \quad (3.5)$$

Multiplying Eq. 3.3 by  $u'_i$  and averaging, yields the evolution of the TKE,  $K = \frac{1}{2} \langle u'_i u'_i \rangle$  (an analytical derivation can be found in e.g., Kundu and Cohen (1990), Chapter 13.7):

$$\begin{aligned} \frac{\partial K}{\partial t} + \langle u_j \rangle \frac{\partial K}{\partial x_j} = & - \frac{\partial}{\partial x_j} \left( \frac{1}{2} \langle u'_i u'_i u'_j \rangle - 2\nu \langle u'_i s'_{ij} \rangle + \frac{\langle u'_j p' \rangle}{\rho_0} \right) \\ & - \langle u'_i u'_j \rangle \frac{\partial \langle u_i \rangle}{\partial x_j} - \frac{g}{\rho_0} \langle w' \rho' \rangle - 2\nu \langle s'_{ij} s'_{ij} \rangle, \end{aligned} \quad (3.6)$$

where  $s'_{ij}$  are the shear tensors for the fluctuating velocities:

$$s'_{ij} = \frac{1}{2} \left( \frac{\partial u'_i}{\partial x'_j} + \frac{\partial u'_j}{\partial x'_i} \right). \quad (3.7)$$

The terms of the left-hand side of the TKE equation (Eq. 3.6) describe the local change in time plus the advection by the mean flow, and together they form the material derivative of  $K$  along the mean flow  $\langle u_i \rangle$ . Moving on to the right-hand side, the three terms inside the parenthesis represent: the transport of TKE by turbulent motions, the viscous transport and the turbulent transport of mechanical energy. Together they describe the total transport of TKE. The term following next is the shear production term and represents the conversion from mean flow to TKE, and vice-versa. If positive, which is usually the case, this term represents the transfer of energy from the mean kinetic energy into the TKE. Next follows the term that represents the turbulent buoyancy flux which can be of either sign. This term describes work against gravity and can be interpreted as the exchange between kinetic and potential energy. In a stably stratified environment, i.e. with  $\frac{-g}{\rho_0} \frac{\partial \bar{\rho}}{\partial z} > 0$ , where  $\bar{\rho}$  is the background density, the turbulent buoyancy flux will lead to a transfer from TKE to potential energy. When turbulent velocity moves a particle upward or downward from its original position, buoyancy forces will tend to bring the particle back to its original position. Hence, the particle will decelerate, and its TKE will be reduced. On the contrary, in case of an unstably stratified environment, i.e. with  $\frac{-g}{\rho_0} \frac{\partial \bar{\rho}}{\partial z} < 0$ , the particle will be further accelerated, and the energy transfer is in the opposite direction. The last term represents the rate of dissipation of TKE into heat, denoted with the symbol  $\epsilon$ , and it is always negative. This term represents the work performed by the small-scale turbulent motions against viscous forces.

In a steady state situation and assuming that TKE is produced locally, the transport term and the time derivative can be neglected, thus Eq. 3.6 becomes a balance between the local turbulent production, the local dissipation into heat and the buoyancy flux (Osborn, 1980):

$$\langle u'_i u'_j \rangle \frac{\partial \langle u_i \rangle}{\partial x_j} = - \frac{g}{\rho_0} \langle w' \rho' \rangle - 2\nu \langle s'_{ij} s'_{ij} \rangle \quad (3.8)$$

The rate of energy removal by buoyancy flux to energy production by shear is defined as the flux Richardson number,  $R_f$ ,

$$R_f = \frac{-\frac{g}{\rho_0} \langle w' \rho' \rangle}{-\langle u' w' \rangle \frac{\partial \langle u \rangle}{\partial z}}, \quad (3.9)$$

and constitutes a dimensionless measure for the net production of TKE. Here the x-axis is oriented in the direction of the flow. As the shear production is usually positive, the sign of  $R_f$  depends on the sign of the buoyancy flux. Therefore, for an unstable environment,  $R_f$  is negative and for a stable environment it is positive. Moreover, for  $R_f > 1$ , the buoyant flux removes turbulence at a larger rate than it is produced by shear, hence the net production of TKE is negative, whereas for  $R_f < 1$  the shear term dominates and the net production is positive.

To conclude, the evolution of small-scale turbulence is determined by the strength of the vertical shear of the background flow and by buoyancy forces due to ambient density stratification. Shear provides a source of kinetic energy for turbulent motion, whereas buoyancy (in stable stratification) damps turbulence (Smyth and Moum, 2000). Another dimensionless number that compares the strength of these effects is the gradient Richardson number,

$$Ri = \frac{N^2}{S^2}, \quad (3.10)$$

where  $N = \left(\frac{-g}{\rho_0} \frac{\partial \rho}{\partial z}\right)^{\frac{1}{2}}$  is the buoyancy frequency (also known as the Brunt-Väisälä frequency), and  $S = \left[\left(\frac{\partial u}{\partial z}\right)^2 + \left(\frac{\partial v}{\partial z}\right)^2\right]^{\frac{1}{2}}$  is the vertical shear. Shear-related instabilities are believed to occur when  $Ri < 0.25$  (Olbers et al., 2012).

## 3.2 Internal Gravity Waves

Waves are generated by a restoring force that tends to bring the system back to its equilibrium state and by some kind of inertia that perturbs the system from its equilibrium state. Ocean waves that have gravity as the restoring force are known as gravity waves. Gravity waves occurring at the surface of the sea are called surface gravity waves, while those occurring at density interfaces within the water column are called internal gravity waves. Internal gravity waves are ubiquitous in the ocean, as well as in the Baltic Sea, and are well known for their contribution to diapycnal mixing (Alford et al., 2016). In the following text, the basic properties of internal gravity waves will be briefly revised.

For a rotating, continuously stratified, inviscid fluid when the Boussinesq approximation is valid and further assuming small wave amplitudes hence, neglecting the non-linear terms, the Navier - Stokes equations reduce to the following equations of motion (Kundu and Cohen, 1990, p. 599):

$$\frac{\partial u}{\partial x} + \frac{\partial v}{\partial y} + \frac{\partial w}{\partial z} = 0, \quad (3.11)$$

$$\frac{\partial u}{\partial t} - fv = -\frac{1}{\rho_0} \frac{\partial p'}{\partial x}, \quad (3.12)$$

$$\frac{\partial v}{\partial t} + fu = -\frac{1}{\rho_0} \frac{\partial p'}{\partial y}, \quad (3.13)$$

$$\frac{\partial w}{\partial t} = -\frac{1}{\rho_0} \frac{\partial p'}{\partial z} - \frac{\rho' g}{\rho_0}, \quad (3.14)$$

$$\frac{\partial \rho'}{\partial t} - \frac{\rho_0 N^2}{g} w = 0, \quad (3.15)$$

Here  $\rho'$  and  $p'$  are perturbations of density and pressure, respectively, from a background state in which the background density  $\bar{\rho}(z)$  and pressure  $\bar{p}(z)$  are assumed to be in hydrostatic balance,

$$\frac{\partial \bar{p}(z)}{\partial z} = -\bar{\rho}(z)g. \quad (3.16)$$

The inertial frequency (or Coriolis parameter) is defined as,  $f = 2\Omega \sin \phi$ , where  $\Omega = 2\pi/(24 \cdot 3600) = 7.29 \times 10^{-5} \text{ s}^{-1}$  is Earth's angular frequency and  $\phi$  is the latitude.

The above system of equations (3.11 - 3.15) consists of: the continuity equation (3.11), the three-dimensional momentum equations (3.12 - 3.14) and the density equation (3.15). The combination of the latter equations, produces the following wave equation (for derivation see App. A):

$$\frac{\partial^2(\nabla^2 w)}{\partial t^2} + N^2 \nabla_H^2 w + f^2 \frac{\partial^2 w}{\partial z^2} = 0, \quad (3.17)$$

where  $\nabla^2$  is the three-dimensional Laplacian operator and  $\nabla_H^2$  is the horizontal Laplacian operator, such that:

$$\nabla^2 \equiv \nabla_H^2 + \frac{\partial^2}{\partial z^2} = \frac{\partial^2}{\partial x^2} + \frac{\partial^2}{\partial y^2} + \frac{\partial^2}{\partial z^2} \quad (3.18)$$

Since the coefficients of (3.17) are independent of the horizontal directions, we can assume a plane wave solution of the form

$$w = w_0 e^{i(kx + ly + mz - \omega t)}, \quad (3.19)$$

where  $k$ ,  $l$ ,  $m$  correspond to the wavenumbers in the  $x$ ,  $y$  and  $z$  directions. Substituting (3.19) into the internal wave equation (3.17), yields the dispersion relation

$$\boxed{\omega^2 = \frac{N^2(k^2 + l^2) + f^2 m^2}{k^2 + l^2 + m^2}}. \quad (3.20)$$

From the dispersion relation, it can be seen that disturbances independent of  $z$ , (i.e. if  $m$  is equal to zero), will oscillate with frequency  $N$ , while disturbances independent of the horizontal position, (i.e.  $k$  and  $l$  are equal to zero), will oscillate at the Coriolis frequency  $f$ , giving rise to two limiting cases. By solving the dispersion relation (3.20) for the vertical wave number, we arrive at the expression

$$m = \sqrt{\frac{(k^2 + l^2)(N^2 - \omega^2)}{\omega^2 - f^2}}, \quad (3.21)$$

which is real only if  $f \leq \omega \leq N$ . Therefore, internal gravity waves are allowed to propagate only between the two characteristic limits, the Coriolis frequency  $f$  and the buoyancy frequency  $N$ .

Another characteristic property of internal gravity waves is that the group propagation is perpendicular to the phase propagation, so that upward phase propagation indicates downward energy propagation (Alford et al., 2016). From the dispersion relation (Eq. 3.20), the group velocity  $\vec{c}_g$  and the phase velocity  $\vec{c}_{ph}$  are calculated as:

$$\begin{aligned} \vec{c}_g &= \frac{\partial \omega}{\partial k} \hat{e}_k + \frac{\partial \omega}{\partial l} \hat{e}_l + \frac{\partial \omega}{\partial m} \hat{e}_m \\ &= \frac{k}{\omega} \left( \frac{N^2}{k^2} - \frac{\omega^2}{k^2} \right) \hat{e}_k + \frac{l}{\omega} \left( \frac{N^2}{k^2} - \frac{\omega^2}{k^2} \right) \hat{e}_l + \frac{m}{\omega} \left( \frac{f^2}{k^2} - \frac{\omega^2}{k^2} \right) \hat{e}_m, \end{aligned} \quad (3.22)$$

$$\vec{c}_{ph} = \frac{\omega}{|k|^2} \vec{k} = \sqrt{\frac{N^2(k^2 + l^2) + f^2 m^2}{(k^2 + l^2 + m^2)^3}} \vec{k}, \quad (3.23)$$

where  $\hat{e}_k, \hat{e}_l, \hat{e}_m$  are the unit vectors in the three Cartesian directions. It follows from Eq. 3.22 and Eq. 3.23 that  $\vec{c}_g \cdot \vec{c}_{ph} = 0$  and hence, the group and phase velocity vectors are perpendicular to each other. Moreover, from the vertical component of the group velocity derived by Olbers et al. (2012) as:

$$c_{gz} = - \left( \frac{N^2 - f^2}{\omega} \frac{k^2 + l^2}{(k^2 + l^2 + m^2)^2} \right) m \hat{e}_m, \quad (3.24)$$

it follows that for  $m > 0$ ,  $c_{gz} < 0$  leading to the fact that the phase and group velocities have opposite vertical components. Therefore,  $m > 0$  ( $m < 0$ ) corresponds to an upward (downward) phase propagation and a downward (upward) group propagation, accompanied by a downward (upward) flux of kinetic energy.

### 3.2.1 Near-Inertial Waves

A substantial fraction of the total ocean internal wave kinetic energy lies near the low frequency end of the spectrum (Alford et al., 2016). These near-inertial internal waves (NIWs) exist almost everywhere in the ocean, except very close to the equator (Kundu, 1993). They are hard to overlook, especially in the tide-less Baltic sea, as they appear as a spectral peak at and just above the local inertial frequency  $f$ <sup>3</sup>. Wind fluctuations with frequencies in the near-inertial band excite inertial motions in the surface mixed layer (Ekman, 1905). Once these motions are generated, horizontal convergences and divergences pump the stratified base of the mixed layer generating NIWs. The short wavelength NIWs propagate vertically into the stratified interior, draining energy from the mixed layer, transferring it to waves of other frequencies via wave-wave interactions, and ultimately depositing it in the form of turbulent mixing (Alford et al., 2016). The faster travelling long wavelength NIWs, on the other hand, propagate hundreds of kilometers away from their source of origin towards the equator and therefore, appear in spectra somewhat higher than the local inertial frequency (Alford et al., 2016). NIWs are characteristic for their nearly circularly polarized horizontal velocities which rotate clockwise in the northern hemisphere with the northward velocity component leading the eastward by 90° and their strong vertical shear. Shear provides a source of kinetic energy and hence, NIWs are considered a major contributor to upper ocean mixing (Alford et al., 2016).

## 3.3 Lateral Variability in the Surface Boundary Layer

The upper ocean is characterized by a surface boundary layer (SBL) that is weakly stratified in density compared to the ocean interior. However, the SBL is not horizontally homogeneous and usually exhibits lateral density gradients associated with large-scale fronts, filaments and eddies, that can significantly modify its depth and structure (Taylor and Ferrari, 2010). These lateral density gradients form at the boundaries of different water masses, upwelling regions and mesoscale eddies, and are significant and sometimes long-lived features of the large-scale structure of the SBL (Thorpe, 2005). Once formed, they are dynamically active and start to tilt from the vertical towards the horizontal (i.e. restratify) under the action of gravity. However, as soon as thermal wind balance is established, Earth's rotation constrains the efficiency of this process and further tilting is hindered (Boccaletti et al., 2007). The thermal wind balance equations are a combination of the geostrophic (Eqs. 3.25 and 3.26) and hydrostatic equations (Eq. 3.27),

---

<sup>3</sup> Technically, motions at frequencies slightly above  $f$  are characterized as NIWs, while motions exactly at the Coriolis frequency are referred to as inertial oscillations. In the latter case, there is no wave motion, just motion of the fluid particles in horizontal near-circular orbits (Kundu, 1993).

$$f u_g = -\frac{1}{\rho_0} \frac{\partial p}{\partial y}, \quad (3.25)$$

$$f v_g = -\frac{1}{\rho_0} \frac{\partial p}{\partial x}, \quad (3.26)$$

$$0 = -\frac{\partial p}{\partial z} - g\rho. \quad (3.27)$$

By eliminating the pressure  $p$  between Eqs. 3.25, 3.27, and between 3.26, 3.27, one obtains the desired thermal wind equations for the zonal and meridional directions, respectively,

$$\frac{\partial u_g}{\partial z} = \frac{g}{\rho_0 f} \frac{\partial \rho}{\partial y}, \quad (3.28)$$

$$\frac{\partial v_g}{\partial z} = -\frac{g}{\rho_0 f} \frac{\partial \rho}{\partial x}. \quad (3.29)$$

The thermal wind relation states that, a horizontal density gradient can persist in steady state if it is accompanied by a vertical shear of horizontal velocity. Therefore, due to the Coriolis force, the system can be maintained in equilibrium, without tendency towards leveling the density surfaces. The resulting equilibrium state is generally unstable; the Coriolis effect can maintain the density distribution in the mean, but any small perturbation will upset the balance locally and restratification will continue. To describe the dynamical role of a balanced lateral density gradient, it is useful to introduce the concept of the Ertel potential vorticity (PV), defined as,

$$q = \vec{\omega}_a \cdot \nabla \left( -\frac{g\rho}{\rho_0} \right). \quad (3.30)$$

Here  $\vec{\omega}_a = f\hat{k} + \vec{\zeta}$  is the absolute vorticity and  $\vec{\zeta} = \nabla \times \vec{u}$  is the relative vorticity. A variety of submesoscale instabilities can develop when PV takes the opposite sign of the Coriolis parameter, i.e.  $f q < 0$ . Submesoscale instabilities have spatial scales of  $\mathcal{O}(1 - 10)$  km and growth scales of  $\mathcal{O}(1)$  day, i.e. they exist at scales intermediate between ML turbulence and mesoscale eddies. Assuming that the Coriolis parameter is positive, a balanced state with negative PV is unstable. PV becomes negative in the presence of a sufficiently strong vertical shear and lateral density gradient and a sufficiently weak vertical density gradient. These conditions may occur within a strong front, with the front providing the vertical shear and lateral density gradient while the SBL is weakly stratified. Which instability arises depends on the gradient Richardson number,  $Ri$ , associated with the vertically sheared balanced flow. Symmetric and baroclinic instabilities are thought to be one of the fastest growing modes. Symmetric instabilities develop when  $0.25 < Ri < 0.95$ . They are independent of the along-front direction and draw their energy from the

thermal wind shear. Baroclinic instabilities, on the other hand, develop when  $Ri > 0.95$  and may arise even when  $f q > 0$ . They are invariant in the cross-front direction and convert available potential energy associated with tilting isopycnals <sup>4</sup> into kinetic energy (Taylor and Ferrari, 2010). The net effect of both instabilities is to lower the center of mass of the fluid and increase the stable stratification in the surface layer. While they convert lateral density gradients into SBL stratification, they promote the downscale energy cascade, supplying energy to turbulence, and thus permitting stratification and turbulence to coexist.

---

<sup>4</sup> Surfaces of constant density.



# Chapter 4

## Study Area and Measurements

### 4.1 Study Area

Hydrographic and turbulence data were obtained in the Eastern Gotland Basin during a research cruise with R/V Elisabeth Mann Borgese in mid-autumn 2017 (16 October - 4 November). The cruise was a joint collaboration of the Leibniz Institute for Baltic Sea Research, Warnemünde and the Helmholtz-Center for Coastal Research, Geesthacht, funded by the German Research Foundation. This thesis is embedded in subproject T2 of the TRR 181 project cluster “Energy transfers in the atmosphere and oceans”, which is devoted to the study of surface-layer turbulence and mixing in the vicinity of density fronts.

The Eastern Gotland Basin, located east of the island of Gotland, is the largest and most central basin of the Baltic Sea with a maximum depth of 259 m and a lateral scale in the order of 100 km (Fig.4.1a). The local inertial period is  $T_f \approx 14.27$  h for a latitude of 57 °N and the corresponding Coriolis frequency is  $f = 2\pi/T_f = 1.22 \times 10^{-4}$  rad s<sup>-1</sup>. The instruments used during the cruise were two Acoustic Doppler Current Profilers (AD-CPs), one facing upwards and the other downwards, mounted on a mooring and deployed at 38 m below sea surface for several days, and a free-falling turbulence microstructure profiler (MSS), deployed directly from the ship. Together, these instruments provided high resolution measurements, both in time and in space. Figure 4.1b shows the location of the mooring (TRR1) and the ship-based transect measurements (TRR101-18). Station TRR1 was located at 57°08’N, 20°32’E and the transects were conducted in the vicinity of the station, covering a length of 5 nm. The deployment time of the mooring and the times of the transect measurements are shown in Fig. 4.2. Time is given in decimal days, starting from midnight of January 1st, 2017, i.e. day 0.5 is 12:00 UTC (Coordinated Universal Time) on January 1st. The local time is +2 UTC until day 300.125 and +1 UTC onward. The mooring was deployed on day 296.3 and recovered on day 305.53. The MSS measurements were conducted during 18 individual transects, some of which were repetitive and hence, categorized into 5 main transects. The MSS measurements started on day 298.56 after the passage of a strong wind event and were completed on day 305.48 but were interrupted for

3.09 days due to passage of a second strong wind event.

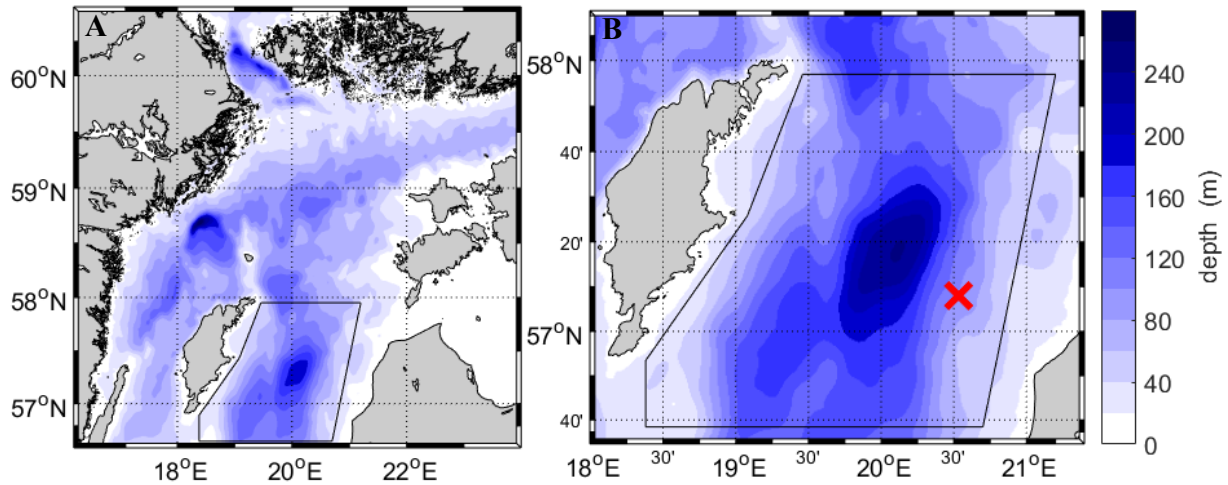


Figure 4.1: Bathymetry maps of the Baltic Sea and the study area: (a) overview map of the Baltic Sea with the Eastern Gotland Basin marked in a box, (b) Eastern Gotland Basin with the location of the mooring, station TRR1, and the ship-based transect measurements, TRR101-18, marked with a red cross. An enlarged version of the measurement area is provided in a later figure.

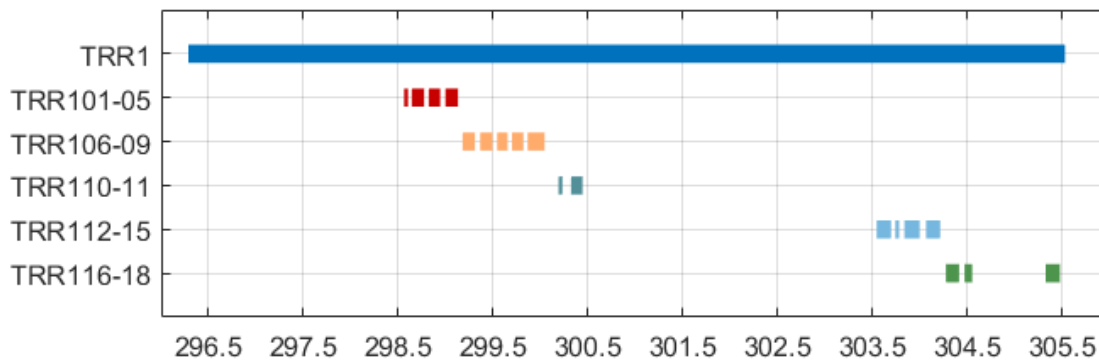


Figure 4.2: Timetable of the mooring (TRR1) and of the MSS transects (TRR101-18). Five main transects were conducted, all of which were repeated several times yielding a total of 18 individual transects.

## 4.2 Moored Measurements

The mooring was deployed at station TRR1 (Fig. 4.1b) on day 296.3, 2.26 days before the microstructure measurements began, and was recovered on day 305.53, right after the

completion of the MSS measurements. The mooring was a combination of an upward and downward facing Acoustic Doppler Current Profiler (ADCP) of 600 kHz and 300 kHz pulse frequency (Teledyne RDI, USA), and a CTD (Conductivity/Temperature/Depth) chain. In the following chapters, only the ADCP data are analyzed and, therefore, the description of the CTD chain is omitted.

### 4.2.1 Acoustic Doppler Current Profilers

The system of ADCPs (Fig. 4.3), mounted at 38 m below sea surface (total depth of the TRR1 station was 94 m), provided vertical profiles of the three velocity components throughout the 9.23 days of its deployment. The operation of the ADCPs was based on the principle of the Doppler effect. Both ADCPs consisted of four circular transducers, tilted by  $20^\circ$  from the vertical and emitting short pulses of high frequency acoustic waves. The sound was partially reflected from particles moving with the water flow. The reflection of a sound pulse in a particular beam was received by the same transducer emitting the sound. Depending on whether the particles were moving towards or away from the transducers, the frequency of the reflected sound was higher or lower than the emitted one. The difference in frequency, the so-called Doppler shift, provided a measurement of the speed of the particles along the beam direction. Furthermore, the distance along the beam from which the sound was reflected, was computed from the speed of sound in seawater and from the travel time of the reflected sound.

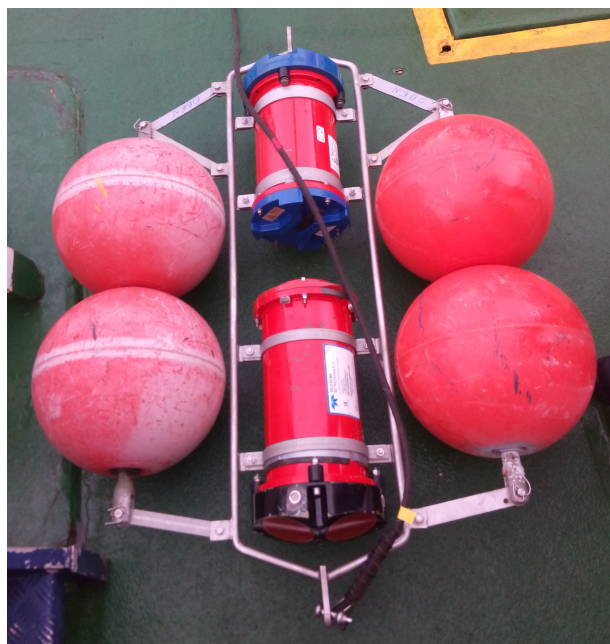


Figure 4.3: Upward and downward facing Acoustic Doppler Current Profiler (ADCP) of 600 kHz and 300 kHz pulse frequency, respectively (Teledyne RDI, USA). The photograph was taken on board of R/V Elisabeth Mann Borgese during the cruise.

The upward facing 600 kHz ADCP sampled the upper part of the water column at 1 s intervals using 1 m bins, with the center of the first bin located at 34.8 m below sea surface. The downward facing 300 kHz ADCP, on the other hand, sampled the lower part of the water column at the same frequency, but using 2 m bins with the center of the first bin located 42.4 m below sea surface. Therefore, apart from the blanking regions near the surface (10 m) and near the bottom (6 m), the two ADCPs provided full depth vertical profiles of the velocity components with a 7.6 m gap between the center of the first bin of each of the two ADCPs. Finally, the velocity estimates were averaged over 1 min to reduce measurement uncertainties.

## 4.3 Ship-Based Measurements

### 4.3.1 Microstructure Measurements

Turbulence microstructure measurements were obtained from a loosely tethered free-falling MSS90-L microstructure profiler (MSS) from In-Situ Wassermesstechnik (ISW, Germany). The MSS profiler was equipped with two airfoil shear probes, a fast responding FP07 temperature sensor, a Seapoint turbidity sensor and high-resolution CTD (Conductivity/Temperature/Depth) sensors. The microscale velocity shear measurements allowed the computation of turbulent dissipation rates, while the fine-scale temperature and conductivity measurements allowed the computation of salinity and density. The profiler's main frame was a 1.25 m long stainless-steel tube with a diameter of 90 mm which weighted 15 kg in air (Fig. 4.4).

The MSS profiler was deployed from the stern of the ship and operated in a yo-yo mode with a sinking speed of 0.5-0.7 m s<sup>-1</sup>, in the vicinity of the TRR1 station (Figs. 4.1b, 4.5). The profiler was connected with a highly flexible electrical cable of about 5 mm outer diameter to a winch that provided sufficient cable slack while the profiler was sinking. This mode of operation allowed the profiler to free-fall and minimized the vibrations during the measuring phase. As the profiler was descending, weights near the bottom and buoyancy elements at the top kept the profiler at a reasonably vertical position. All sensors were mounted at the bottom of the instrument within a cone-shaped protection cage (Fig. 4.4), in order to measure the fluctuations in the undisturbed water below the profiler and thus, making it possible to obtain vertical profiles as deep as 0.1 m above sea bottom. Furthermore, horizontal components of acceleration were also recorded to differentiate real from body-induced fluctuations and to make appropriate corrections. The sampling rate for all sensors on the MSS profiler was 1024 Hz and the data were transmitted from the profiler through the electrical cable to a unit on board and then to a data acquisition computer. Once the profiler reached sea bottom, it was pulled back up to surface and the new cast started immediately. After reducing the noise from all data, (the procedure is not analyzed in this thesis), the CTD data were then averaged into 0.1 m vertical bins, while the dissipation rate data were averaged into 0.5 m vertical bins. The noise level of the profiler is of  $\mathcal{O}(10^{-9})$  W kg<sup>-1</sup>.

The dissipation rate data, as mentioned above, were estimated from the airfoil shear probes mounted at the end of a cylindrical shaft. The measuring principle of the shear probes is explained in detail by Prandke and Stips (1998). The main idea is that the transverse components of turbulent velocity produce a lift force at the airfoil probe. A piezoelectric crystal, embedded within the airfoil probe, senses the lift force and induces a voltage which is proportional to the instantaneous horizontal component of the velocity field. When the small-scale shear is estimated from the voltage output, the dissipation rate of turbulent kinetic energy  $\epsilon$  can be calculated according to its definition (see Ch. 3.1.1):

$$\epsilon = 2\nu \langle s'_{ij} s'_{ij} \rangle. \quad (4.1)$$

Here  $\nu$  is the molecular viscosity and  $s'_{ij}$  is the nine-component strain tensor for the fluctuating velocity components ( $u'_1, u'_2, u'_3$ ) in the three orthogonal directions ( $x_1, x_2, x_3$ ):

$$s'_{ij} = \frac{1}{2} \left( \frac{\partial u'_i}{\partial x_j} + \frac{\partial u'_j}{\partial x_i} \right). \quad (4.2)$$

The dissipation rate  $\epsilon$  quantifies the loss of turbulent kinetic energy in a fluid to heat due to molecular viscosity  $\nu$ . According to Kolmogorov's theory (Kolmogorov, 1941), for sufficiently high Reynolds numbers  $Re = UL/\nu$ , where  $U$  is the velocity scale and  $L$  is the length scale (see Ch. 3.1), the small-scale turbulent motions are statistically isotropic, i.e. invariant against arbitrary coordinate translations, rotations and reflections, and depend on only two parameters, the viscosity and the dissipation rate. On dimensional grounds, he derived that the smallest scales must be of size  $\eta = (\nu^3/\epsilon)^{1/4}$ , which is now known as the Kolmogorov length scale<sup>1</sup>. Hence, the nine-component strain tensor (Eq. 4.2), assuming local isotropy, reduces to a single microscale shear component such that:

$$\epsilon = \frac{15}{2} \nu \left\langle \left( \frac{\partial u'}{\partial z} \right)^2 \right\rangle. \quad (4.3)$$



Figure 4.4: Free falling MSS90-L microstructure profiler (MSS). The photograph was taken on board of R/V Elisabeth Mann Borgese during the cruise.

<sup>1</sup> The oceanic values of  $\epsilon$  lead to a range of  $\eta$  from about  $6 \times 10^{-5}$  m in very turbulent regions to 0.01 m in the abyss.

The vessel was cruising with a speed of 1-2 kn against the wind to prevent the profiler from moving under the ship, along 5 main predefined transects of approximately 5 nm length, each of which was repeated several times leading to a total number of 18 individual transects (Fig. 4.5). At the end of each transect, measurements were shortly interrupted until the ship was re-positioned at the downwind end of the transect or moved on to another transect. Depending on the water depth, a complete water column profile was obtained approximately every 5 min and depending on the sea state and local weather conditions, each transect required 1-2 hours to be completed. Overall, 547 profiles in 18 transects were obtained, 323 of which (11 transects) were obtained after the first wind event and 224 (7 transects) after the second wind event, providing a detailed vertically resolved picture of stratification and mixing parameters inside and below the surface mixed layer in the study area.

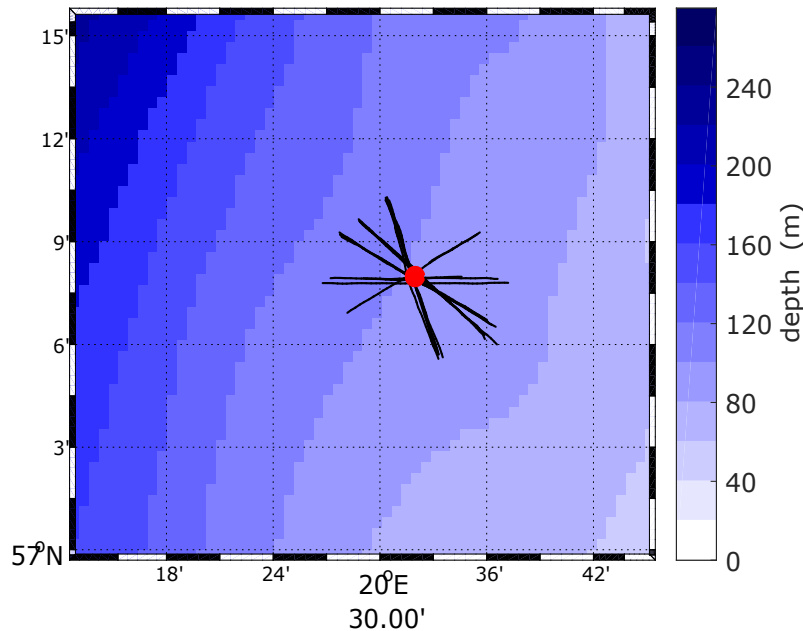


Figure 4.5: Map of the mooring position, station TRR1 (red dot) and the MSS transects, TRR101-18 (black lines).

### 4.3.2 Meteorological data

Wind speed and direction were obtained from the meteorological station mounted on the research vessel with a sampling interval of 10 s. However, due to two strong wind events, R/V Elizabeth Mann Borgese had to seek shelter against the severe weather conditions and measurements were not recorded from days 296.5 to 298.5 and 300.42 to 303.5. For the following analysis, data from Germany's National Meteorological Service, the Deutscher Wetterdienst (DWD), were used to fill in the gaps. From the comparison of the available

ship-based wind data and the DWD data (Fig. 4.6), it was concluded that the data sets were in sufficient agreement for the purpose of the following chapters and, consequently, the wind data used for the analysis of the ADCP and MSS data was based solely on the DWD data.

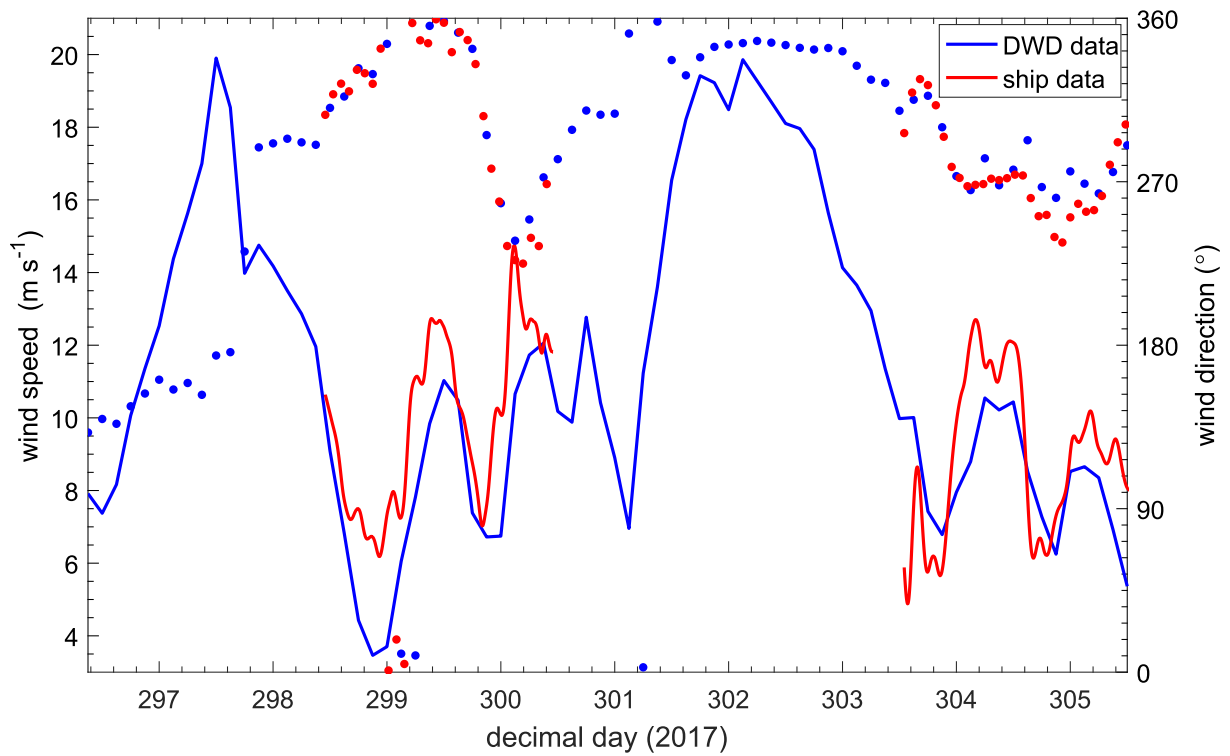


Figure 4.6: Time series of wind speed (lines) and direction (dots). In blue is the data obtained from Germany’s National Meteorological Service, the Deutscher Wetterdienst (DWD), and in red is the data obtained from the meteorological station mounted on R/V Elisabeth Mann Borgese.



# Chapter 5

## Observations

### 5.1 Current Structure in the Eastern Gotland Basin

The eastward and northward velocity time series in Fig. 5.1, obtained from the upward and downward facing system of ADCPs (see Ch. 4.2.1), provide a general overview of the current velocity structure at station TRR1 in the Eastern Gotland Basin (Fig. 4.1) during the 9.23 days of the mooring's deployment. Panel (A) of the figure presents the wind speed and direction obtained from DWD (see Ch. 4.3.2), panel (B) presents the time series of the eastward velocity component and panel (C) presents the time series of the northward velocity component. Concentrating on panel (A), one can easily discern two strong wind events of almost the same speed but of opposite directions. During the first wind event (day 297 to 298.5), the winds were blowing from a southern direction and reached a maximum speed of  $20 \text{ m s}^{-1}$  on day 297.8. During the second wind event (day 301.5 to 303), the winds were blowing from a northern direction and reached a maximum speed of  $19.86 \text{ m s}^{-1}$  on day 302.1. These wind events are associated with opposite Ekman transports as reflected in the current data (panels (B) and (C)). According to Ekman's theory (Ekman, 1905), the Earth's rotation and frictional forces deflect the net transport of water  $90^\circ$  to the right of the direction of the wind in the northern hemisphere. Due to the prevailing southerly winds of the first wind event, the Ekman transport forces the surface waters to move towards the Latvian coast to the east, where they converge and sink. This process is known as downwelling and leads to a temporal deepening of the halocline. At the end of the first wind event, around day 298.5, the halocline rises back to its equilibrium position. The persistent northerly winds of the second wind event, lead to the opposite phenomenon. The resulting Ekman transport forces the surface waters to move towards the west, decelerating the upper water column which was accelerated during the previous wind event.

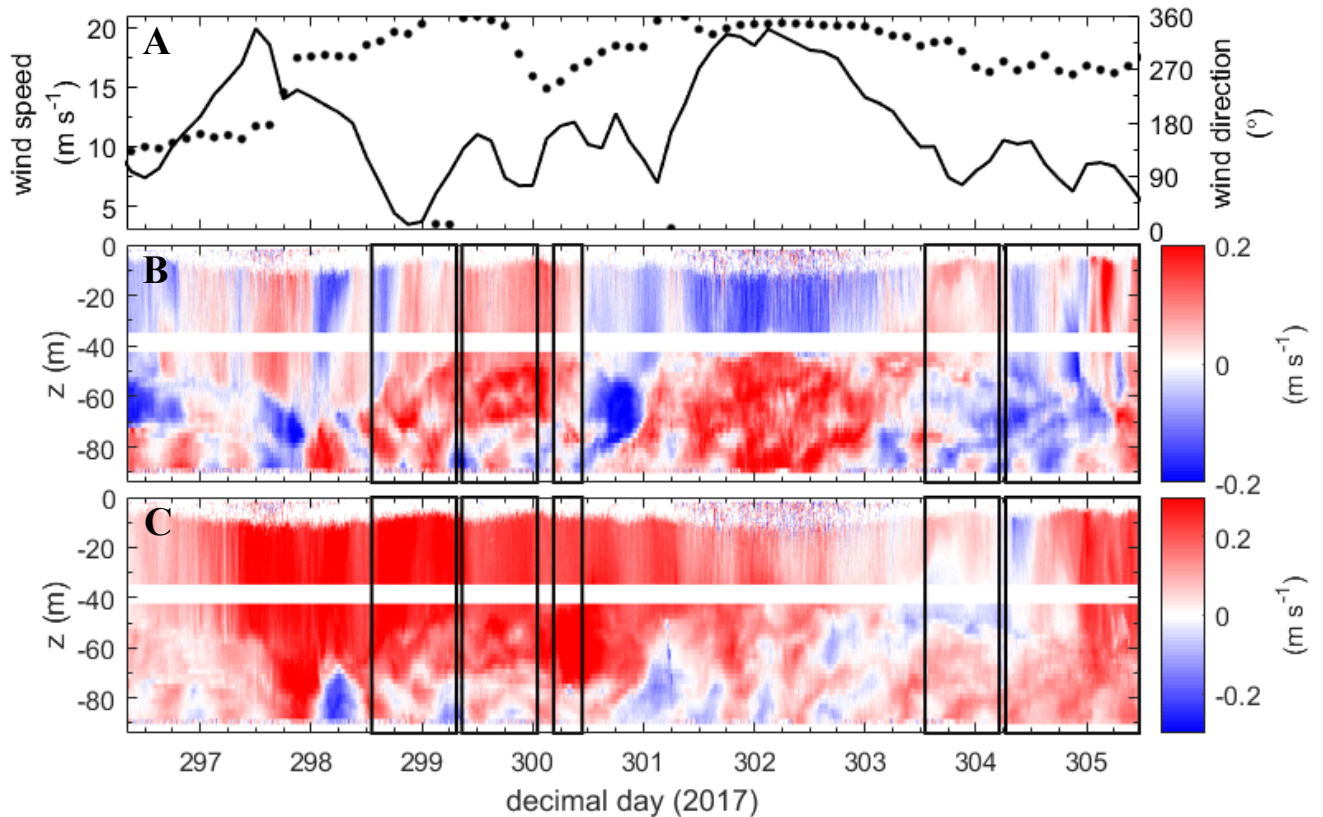


Figure 5.1: Time series of (A) wind speed (lines) and wind direction (dots), time series of unfiltered (B) eastward and (C) northward velocity components from the moored ADCPs, providing an overview of the velocity structure at station TRR1. Black rectangles mark the periods of the microstructure measurements. Note that the color range is not consistent in all panels.

### 5.1.1 Near- $f$ Wave Motions

For the analysis of the vertical structure of the observed velocities, the eastward and northward velocity components were decomposed into an internal and a sub-inertial wave band contribution. Following [Van der Lee and Umlauf \(2011\)](#), the current fluctuations in the sub-inertial range were computed by low-pass filtering the original current measurements using a sixth-order phase-preserving Butterworth filter with a cut-off period of 20.68 h, equivalent to a cut-off frequency of  $1.34 \times 10^{-5} \text{ s}^{-1} = 0.7f$ . The current fluctuations in the internal wave band were computed by subtracting the latter low-pass filtered velocities from the original measurements, i.e. by high-pass filtering. (A brief analysis on numerical filtering is provided in App. B.)

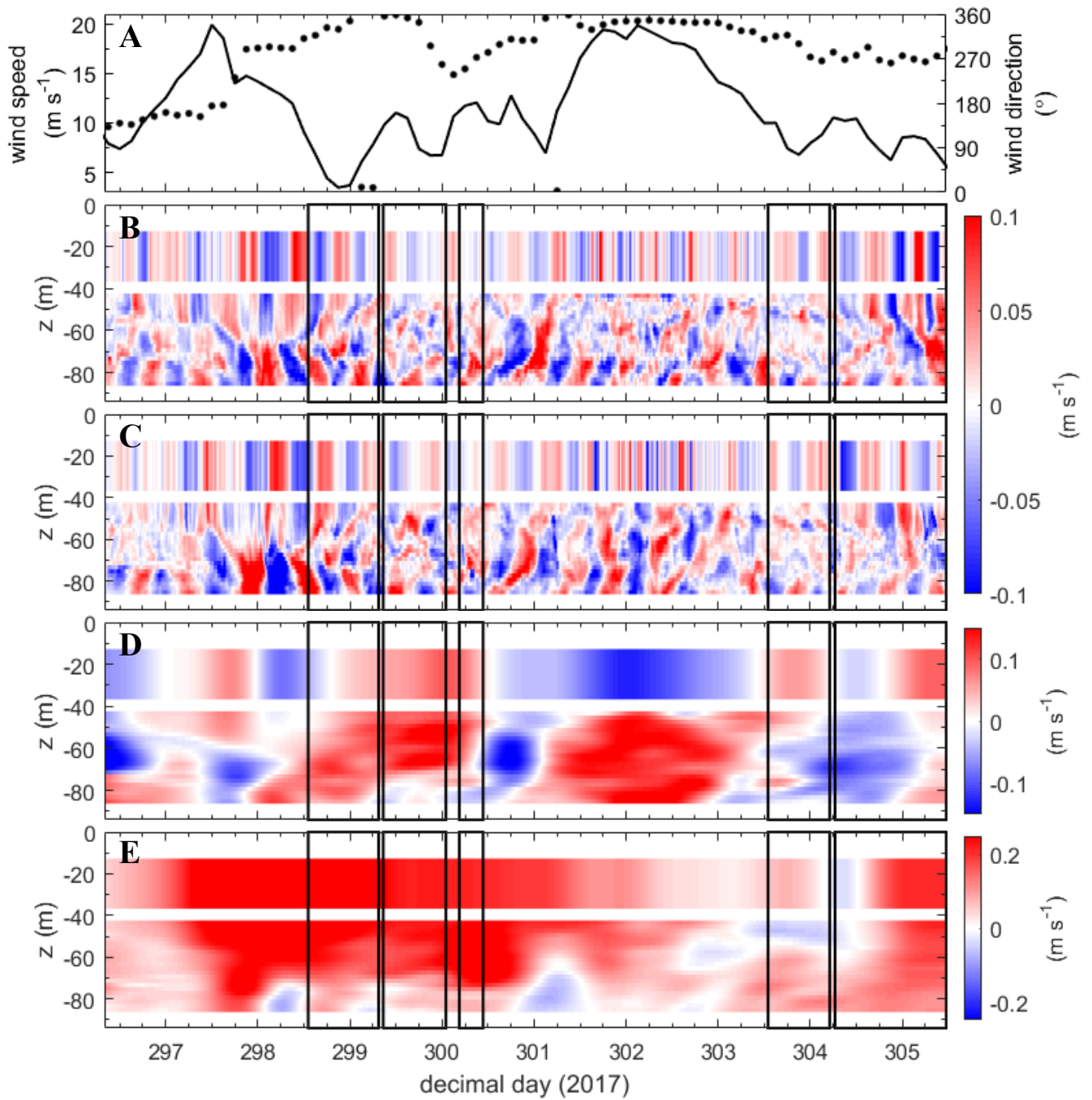


Figure 5.2: Time series of (A) wind speed (lines) and wind direction (dots), time series of high-pass filtered (B) eastward and (C) northward velocity components, time series of low-pass filtered (D) eastward and (E) northward velocity components. The data were measured at station TRR1 and filtered with a sixth-order phase preserving Butterworth filter with a cutoff period of 20.67 h. Black rectangles mark the period of the microstructure measurements. Note that the color range is not consistent in all panels.

The filtered velocities observed during the period of the deployment of the ADCPs at station TRR1, are shown in Fig. 5.2. Velocities in the internal wave band (Fig. 5.2, B and C) are dominated by clockwise rotating near-inertial motions. The clockwise rotating winds during the first wind event (days 297-298.5) generate strong near-inertial currents, especially visible during day 298 in the upper part of the water column. Moreover, evident is the presence of near-inertial waves just below the halocline (65 m depth), during the same day. The tilt of the phase lines in this region is an indication of downward phase propagation and, consequently, of upward energy flux propagation, suggesting that the latter observed NIWs were locally generated at the topographic slope close to the mooring. These waves may have originated at the intersection of the halocline with the sloping bottom during the readjustment process of the halocline to its equilibrium position (see Ch. 5.1). Furthermore, the out of phase motions above and below the halocline, lead to the generation of a strong vertical shear layer. If the shear is strong enough, specifically if the Richardson number  $Ri = N^2/S^2$  is less than 0.25 (see Ch. 3.1.1), shear-related instabilities will potentially cause local mixing. The mixed layer can be identified as a region of low vertical shear, while the bottom of the mixed layer is visible as a region of high vertical shear. After the wind event, the wind speed decreases and the near-inertial motions are attenuated. From day 300.2 and for the next 48 hours, while the near-inertial motions in the surface mixed layer remain weak, near-inertial energy levels are observed in the layers below the halocline, causing vertical shear at the bottom of the mixed layer. The fact that the phase lines in the deeper layers show an increasing tilt, indicates upward phase propagation and consequently, downward energy flux. Since wind speeds are relatively low during this period, it is likely that these motions have resulted from the delayed arrival of higher internal wave modes, generated by the wind in the mixed layer near the lateral boundaries (Kundu et al., 1983; Van der Lee and Umlauf, 2011). As the waves arrive with a delay of 3-4 days after the wind event, these boundaries must be located far from the mooring, possibly on the Gotland coast. During the second wind event, the relatively steady northerly winds, break down the near inertial motions.

Further support for these findings is provided by the extracted time series of the eastward and northward velocity components, for 22.76 m and 72.36 m depth, where the stronger near-inertial signals are observed (Fig. 5.3). The latter signals were filtered with a sixth-order phase-preserving band-pass Butterworth filter, to retain frequencies between  $0.7f$  and  $1.3f$  and to reduce the noise from higher frequency signals. As seen in Fig. 5.3, in both depths, the northward velocity component is leading the eastward by  $90^\circ$ , consistent with the expected clockwise rotation of NIWs in the northern hemisphere. The horizontal velocities of the 22.76 m depth (panels (B) and (C)), follow the fluctuations of the winds (panel (A)); the first wind event gives rise to near-inertial waves, which reach a maximum amplitude of approximately  $0.1 \text{ m s}^{-1}$ , while the second wind event attenuates them. The horizontal velocities at 72.36 m depth (panel (D) and (E)), on the other hand, present stronger signals and follow a different pattern than the velocities at 22.76 m depth. Maximum velocities, as in the surface layer case, are observed during the first wind event, but with amplitudes of about  $0.22 \text{ m s}^{-1}$ , i.e. double the amplitude of the velocities in the mixed layer. A less strong signal of  $0.14 \text{ m s}^{-1}$  amplitude is observed right before the

second wind event, while a weaker signal, which was not very clear in Fig 5.2, B and C, of amplitude less than  $0.1 \text{ m s}^{-1}$ , is observed during day 303.

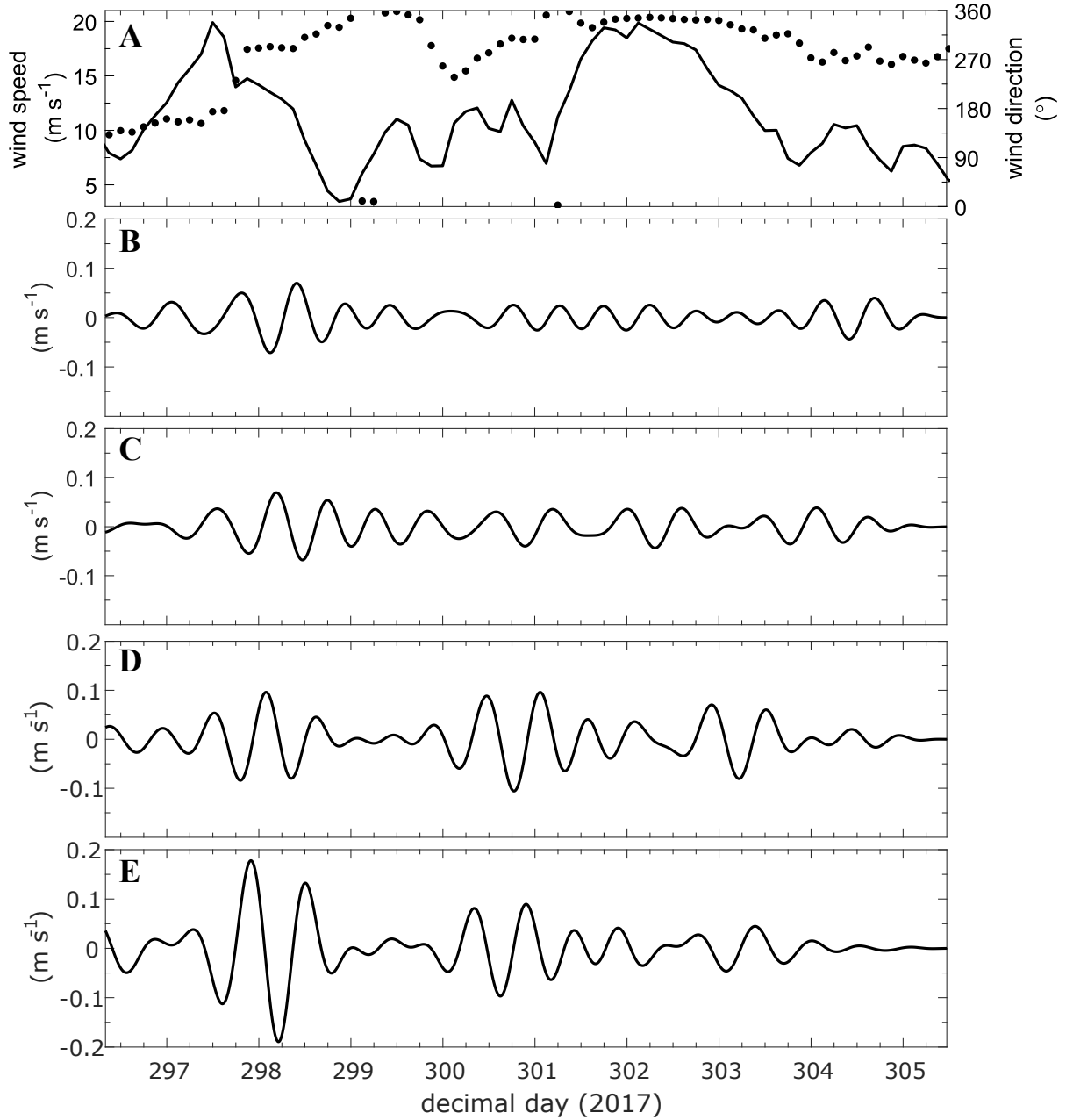


Figure 5.3: Time series of (A) wind speed (lines) and wind direction (dots), time series of band-pass filtered: (B) eastward and (C) northward velocity components for 22.76 m (D) eastward and (E) northward velocity components for 72.36 m at station TRR1.

Moreover, when plotting the power spectra in the frequency domain for the unfiltered eastward and northward velocity time series (Figs. 5.4), other than the expected well-defined peak at and just above the local inertial frequency,  $f$ , one can see that the current signals below the halocline are stronger than the signals in the surface layer. However, for periods less than 0.1 days (or 2.4 hours), the surface energy levels start exceeding those in the halocline. This could be an indication of the existence of submesoscale motions which will be briefly discussed in Ch. 5.3.

Finally, the temporal evolution of the sub-inertial velocity is shown in Fig. 5.2, D and E. These slowly varying signals provide a sub-inertial contribution to the total shear that may be significant for small-scale internal wave motions and mixing.

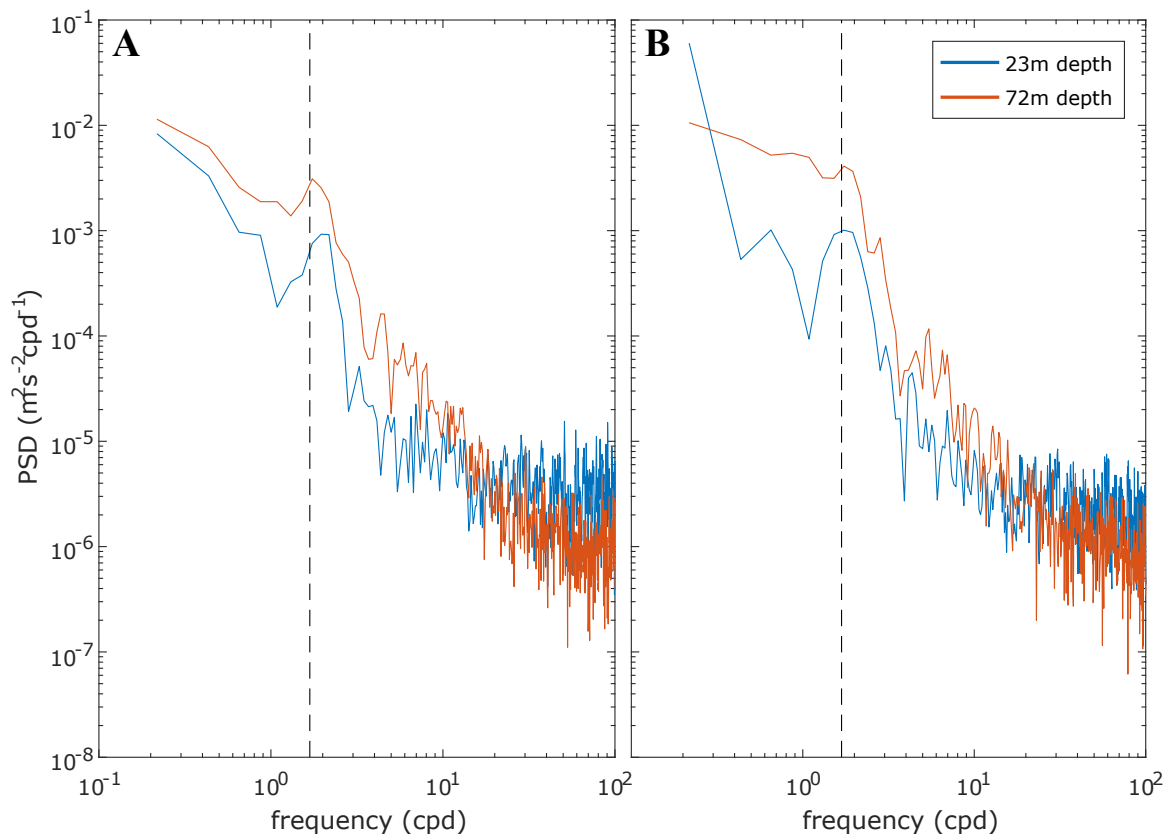


Figure 5.4: Power spectra of (A) eastward and (B) northward velocity components at 22.76 m (in blue) and 72.36 m (in red) depth at station TRR1. The inertial frequency,  $f = 1.68$  cpd (cycles per day), is marked with a dashed line.

## 5.2 Dissipation Measurements

The analysis of the dissipation measurements in the vicinity of station TRR1 is based on 547 microstructure (MSS) profiles, conducted during the periods marked in bold rectangles in Figs. 5.1 and 5.2. In each of the marked periods, the vessel repeated a specific and predefined transect, hence, measurements were collected over 5 main transects (see Fig. 4.5). Specifically, 323 MSS profiles (obtained during 11 individual transects or 3 main transects), were conducted after the first wind event, between days 298.55 and 300.45, and the remaining 224 profiles (obtained during 7 individual transects or 2 main transects) were conducted after the second wind event, between days 303.54 and 305.48, with a gap of 18.45 h after day 304.55 (see Ch. 4.3.1). Therefore, the MSS measurements are grouped into two periods; period I includes all measurements acquired after the first wind event and period II includes all measurements acquired after the second wind event. The winds during both periods were coming from the west and were fluctuating between  $3.5 \text{ m s}^{-1}$  and  $12 \text{ m s}^{-1}$  during the first period, and between  $6.2 \text{ m s}^{-1}$  and  $10.5 \text{ m s}^{-1}$  during the second period.

### 5.2.1 Stratification Parameters

The vertical profiles of the stratification parameters, including conservative temperature <sup>1</sup>, absolute salinity <sup>2</sup>, potential density <sup>3</sup> and buoyancy frequency squared, based on the average of the corresponding MSS profiles over each of the two periods, are summarized in Fig. 5.5. A nearly well-mixed surface layer of approximately 45 m thickness is evident, with an average temperature of  $11.5 \text{ }^\circ\text{C}$  during period I and  $10.6 \text{ }^\circ\text{C}$  during period II, and an average salinity of  $7.5 \text{ g kg}^{-1}$  during both periods. In period I, the mixed layer is bounded from below by a thin thermocline centered at slightly above 50 m depth, followed by a thick halocline, centered at about 70 m depth, which gradually merges into the stratified lower part of the water column. In period II, the thermocline and the halocline coincide, with the halocline extending from 45 m to 75 m depth. Therefore, the thermocline is almost completely eroded and what is visible in period I is simply the remnants of the previous season. The different levels of the halocline are a result of the opposite Ekman transports that took place during the “opposite” wind events, as described in Ch. 5.1. The downwelling during the first wind event lead to a deepening of the halocline and the upwelling during the second wind event, to a rise. However, the upwelling during period II coincided with the erosion of the halocline from the top due to mixed layer turbulence (discussed in Ch. 5.3), preventing it to rise above 45 m depth. Variations of potential density caused by the observed distribution of temperature and salinity are

<sup>1</sup> Defined as potential enthalpy divided by the fixed heat capacity,  $c_p^0 \equiv 3991.87 \text{ J kg}^{-1}\text{K}^{-1}$ ; it accurately represents the heat content per unit mass of seawater,  $T[^\circ\text{C}]$ . Potential enthalpy is the enthalpy a water parcel would have if it were moved adiabatically, i.e. without heat or mass exchange with its surroundings, to the sea surface. (IOC et al., 2010)

<sup>2</sup> Mass fraction of salt in seawater,  $S[\text{g kg}^{-1}]$ .

<sup>3</sup> The density a water parcel would have if it were moved adiabatically to the sea surface,  $\rho_\theta[\text{kg m}^{-3}]$ .

illustrated in Fig. 5.5C. Both the thermocline and the halocline are mirrored in two density interfaces for period I, with the lower being more pronounced, while for period II, during which the halocline and the thermocline coincide, the density profile mirrors exactly the halocline profile. Moreover, the buoyancy frequency squared (Fig. 5.5D) is highest inside the halocline, reaching a maximum of  $1.6 \times 10^{-3} \text{ s}^{-2}$  at 73.5 m depth in period I, and  $1.32 \times 10^{-3} \text{ s}^{-2}$  at 48 m depth in period II. In period one, the buoyancy frequency squared presents a second maximum inside the thermocline, reaching values of  $0.963 \times 10^{-3} \text{ s}^{-2}$  at 46.5 m depth. On the other hand, stratification is almost non-existent in the nearly well-mixed surface layer and weak below the halocline, during both periods, and in the second period, stratification is weak inside the layer between the two pycnoclines as well. Furthermore, the slightly increasing temperature inside and just below the halocline (Fig. 5.5A) is a result of warm and salty waters intruding from the North Sea.

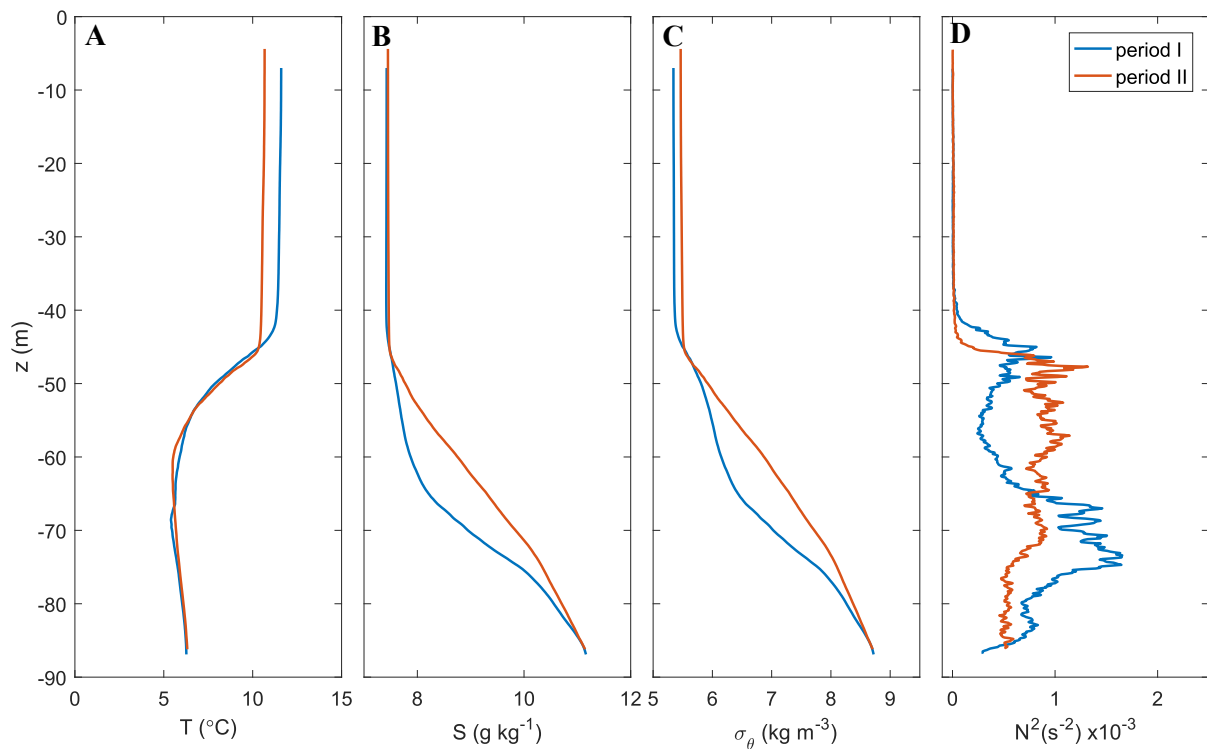


Figure 5.5: Vertical profiles of (A) conservative temperature, (B) absolute salinity, (C) potential density,  $\sigma_\theta = \rho_\theta - 1000 \text{ kg m}^{-3}$ , and (D) buoyancy frequency squared, in the vicinity of station TRR1. Blue profiles correspond to the average of 323 MSS profiles obtained after the first wind event (period I, days 298.55 to 300.45), and red profiles correspond to the average of 224 profiles obtained after the second wind event (period II, days 303.54 to 305.48).

### 5.2.2 Mixing Parameters

The temporal evolution of the wind, conservative temperature, absolute salinity, buoyancy frequency squared and dissipation rate, with contours of potential density superimposed in all subplots, for the periods after the first and second wind event, is illustrated in Figs. 5.6 and 5.7. The dissipation rate time series (Figs. 5.6E and 5.7E), indicate three layers of enhanced turbulence; a surface layer, an interior layer located inside and just below the strongly stratified halocline (also observed in the thermocline during period I although weaker) and a bottom layer. The highest dissipation rates, of  $\mathcal{O}(10^{-7})$  W kg<sup>-1</sup>, are observed in the surface layer above the halocline and are directly related to wind forcing at the sea surface. Turbulence in the upper layer follows closely the variability of the wind throughout the period of the MSS measurements. The measured dissipation is maximum near the sea surface and gradually decreases towards the base of the layer. On the other hand, turbulence in the stratified interior, observed as intermittent patches of enhanced dissipation inside and just below the halocline (and the thermocline during the first period), is not directly related to wind forcing. The permanent tendency for surface layer restratification (Figs. 5.6D and 5.7D) and the strongly stratified, deep halocline prevent the surface layer turbulence to reach the interior layer. According to [Lass et al. \(2003\)](#), wind speeds greater than 14 m s<sup>-1</sup> are required for wind-driven turbulence to erode the halocline. The filtered vertical structure of the eastward and northward velocity components obtained from the moored ADCPs (Fig. 5.2), indicates that near-inertial, as well as sub-inertial shear, is discerned at the bottom of the surface boundary layer and at regions with vertical phase propagation, particularly evident in the lower part of the water column. Therefore, the patches of enhanced dissipation rates seen inside the halocline (Figs. 5.6E and 5.7E) could be energized by shear instabilities due to internal and sub-inertial wave motions, as suggested by [Van der Lee and Umlauf \(2011\)](#). Moreover, turbulence directly above and below these energetic patches is seen to be weak, with dissipation rates reaching values of  $\mathcal{O}(10^{-9})$  W kg<sup>-1</sup> which is approximately the noise level of the MSS profiler. Finally, turbulence in the bottom layer is significantly weaker compared to turbulence observed in the surface layer. Turbulence in this layer could be driven by near-inertial shear within the frictional boundary layer ([Lappe and Umlauf, 2016](#)). However, there is no clear indication of a well-mixed bottom layer due to the permanent tendency for bottom layer restratification resulting from the sloping topography.

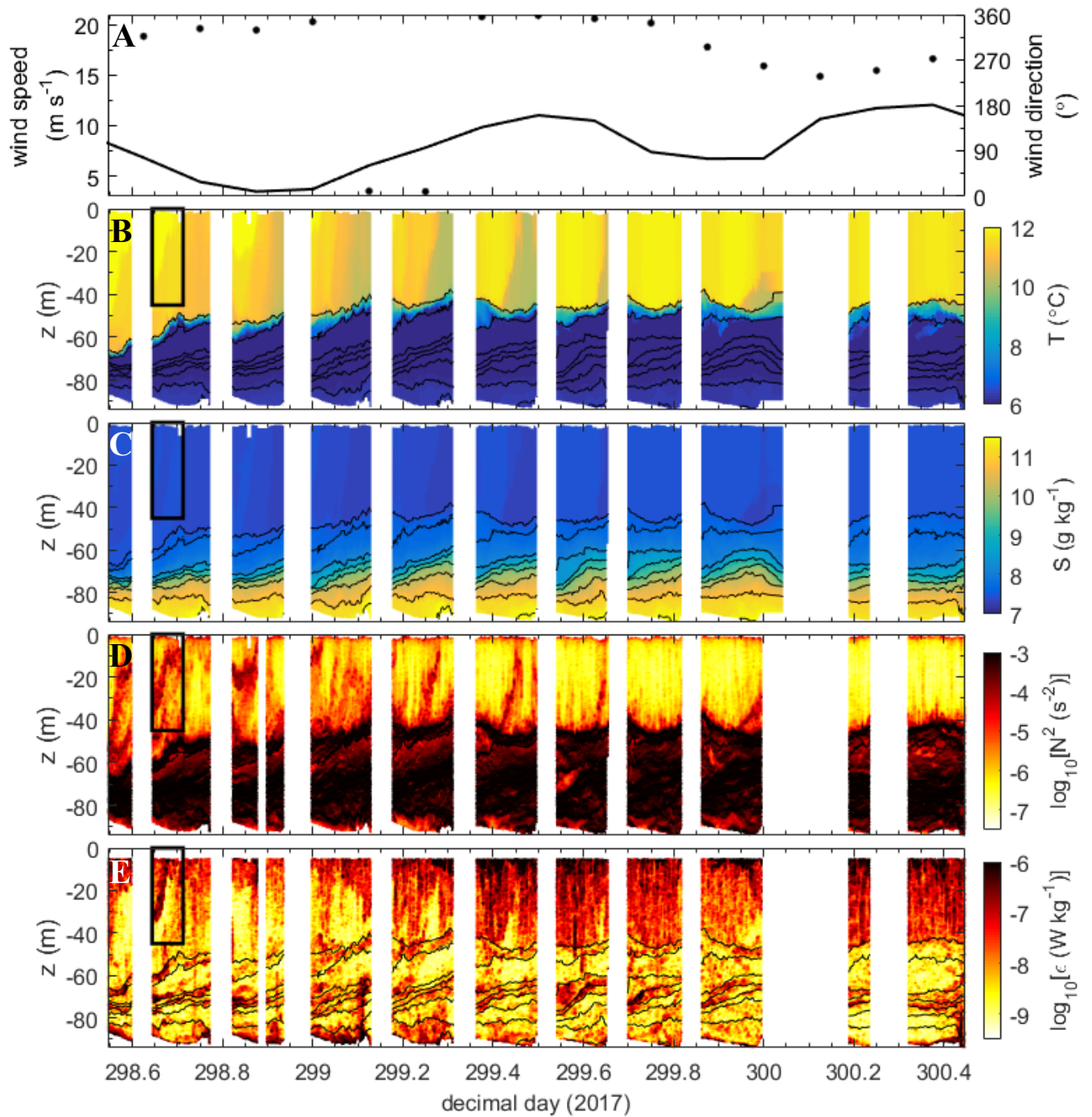


Figure 5.6: Time series of (A) wind speed (lines) and wind direction (dots), (B) conservative temperature, (C) absolute salinity, (D) buoyancy frequency squared and (E) dissipation rate, obtained from the MSS measurements conducted in the vicinity of station TRR1 after the first wind event. Black contour lines denote density isopycnals. The black rectangle marks the enlarged plots of the second transect provided and discussed in the next section.

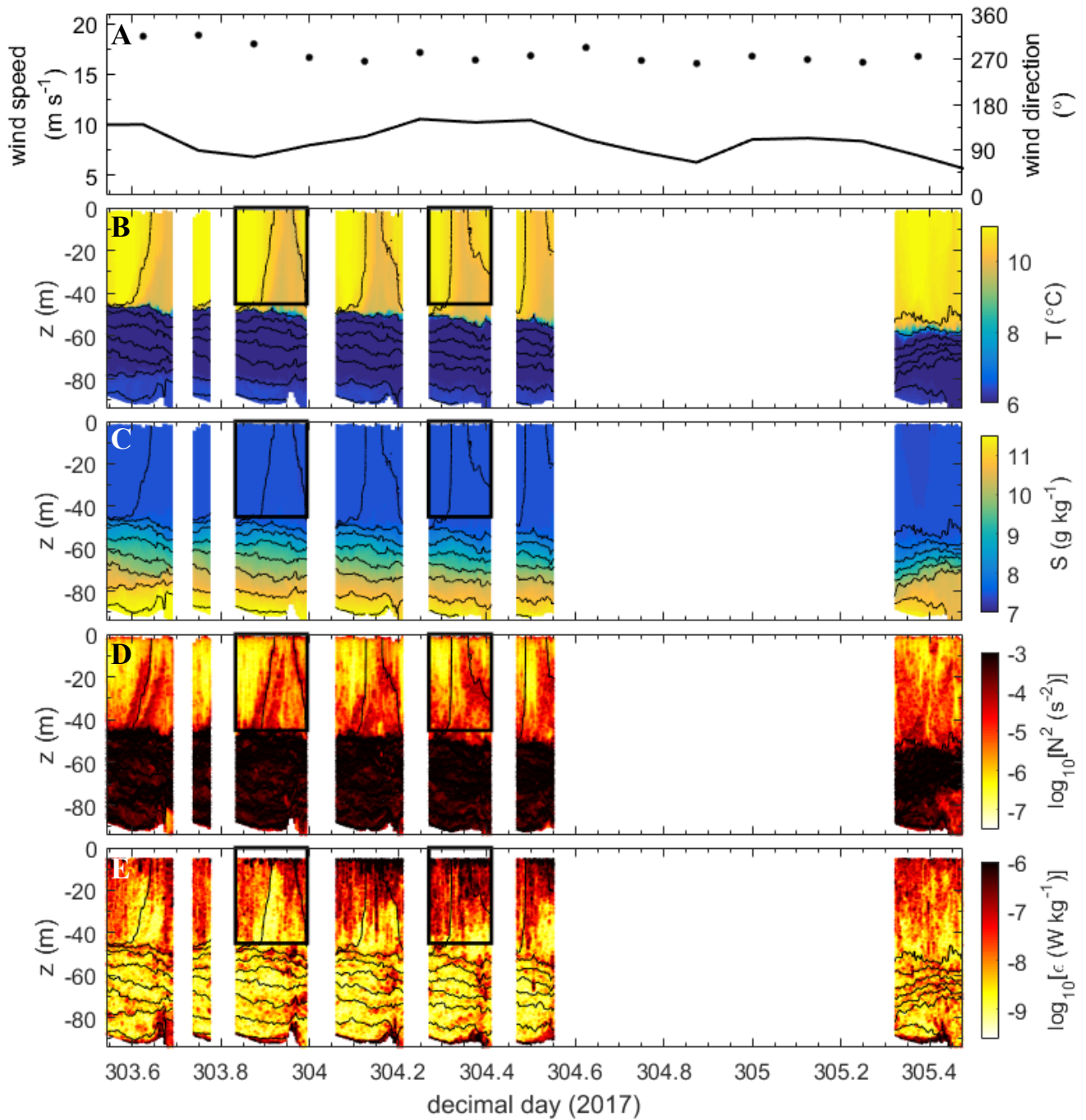


Figure 5.7: Time series of (A) wind speed (lines) and wind direction (dots), (B) conservative temperature, (C) absolute salinity, (D) buoyancy frequency squared and (E) dissipation rate, obtained from the MSS measurements conducted in the vicinity of station TRR1 after the second wind event. Black contour lines denote density isopycnals. Black rectangles mark the enlarged plots of the third and fifth transect provided and discussed in the next section.

## 5.3 Turbulence in the Surface Boundary Layer

As opposed to the general overview of the stratification and mixing parameters given in the previous sections, the focus of this section is on the surface boundary layer (SBL). The SBL is seen as a weakly stratified layer in the upper 45 m of the water column, overlying the stratified interior (panel (D) in Figs. 5.6, 5.7). However, focusing on panels (B) and (C) of Figs. 5.6, 5.7, one can discern horizontal temperature and salinity gradients. These lateral density gradients, associated with fronts and filaments, significantly modify the structure of the SBL, as seen in the following examples.

The first example is of a strongly stratified whilst turbulent front observed between days 298.645 and 298.71 (marked in a box in Fig. 5.6 and then enlarged in Fig. 5.8). This almost vertical region of turbulence seen in the dissipation rate plots (panels (E) and (D)), is not surface generated; it is spawned at 35 m depth in the beginning of the second transect and increases towards the surface. This indicates that turbulence in this case developed inside the front. After the passage of the wind event, an adjustment process takes place that restratifies the surface layer by tilting the nearly vertical isopycnals. This slumping, initially a simple gravitational overturning, is subsequently modified by the Coriolis force leading to a geostrophic adjustment in which the flow will adjust to a state of geostrophic balance (Rossby, 1938). According to Tandon and Garrett (1994), the vertical shear of the horizontal velocity driven by the density gradient, could be strong enough to destabilize the flow and result in mixing. This could explain the turbulent patch seen in the second transect.

The second example concerns a cold filament wedged between two fronts observed during period II, especially visible between days 303.85 and 304.55 (Fig. 5.7B). Taking, for instance, the third and fifth transect of period II (marked in boxes in Fig. 5.7 and then enlarged in Fig. 5.9), one can conclude that the structure of the isopycnals in the magnified plots indicates that the filament is denser than its surroundings and the salinity structure intensifies the density anomaly. The contradicting effects of low ( $7 \text{ m s}^{-1}$ ) and high ( $10 \text{ m s}^{-1}$ ) winds (Fig. 5.7A) on the filament, reflected in the different isopycnal structure are evident. During the first half of the third transect, the wind speed remains low and the filament appears strongly stratified with no evidence of turbulence. During the second half of the transect, the wind speed starts to increase and as a result, stratification decreases and elevated dissipation rates appear in regions of relatively weak stratification (Fig. 5.9, C1 and D1). During the fifth transect, however, the high wind speed does not have the expected effect. In this case, the filament appears strongly stratified with the isopycnals almost horizontally tilted, and in the meantime, turbulent (Fig. 5.9, C2 and D2). This paradoxical coexistence of turbulence and vertical density gradients may be related to submesoscale instabilities created within the filament. Whitt and Taylor (2017) used large-eddy simulations to study the coupled response of submesoscale instabilities and small-scale turbulence to the passage of an idealized autumn storm. They found that submesoscales maintain strong mean stratification in the SBL even during strong down-front winds. The authors suggested that the winds simultaneously energize small-

scale turbulence and submesoscales which could explain the situation observed in the fifth transect.

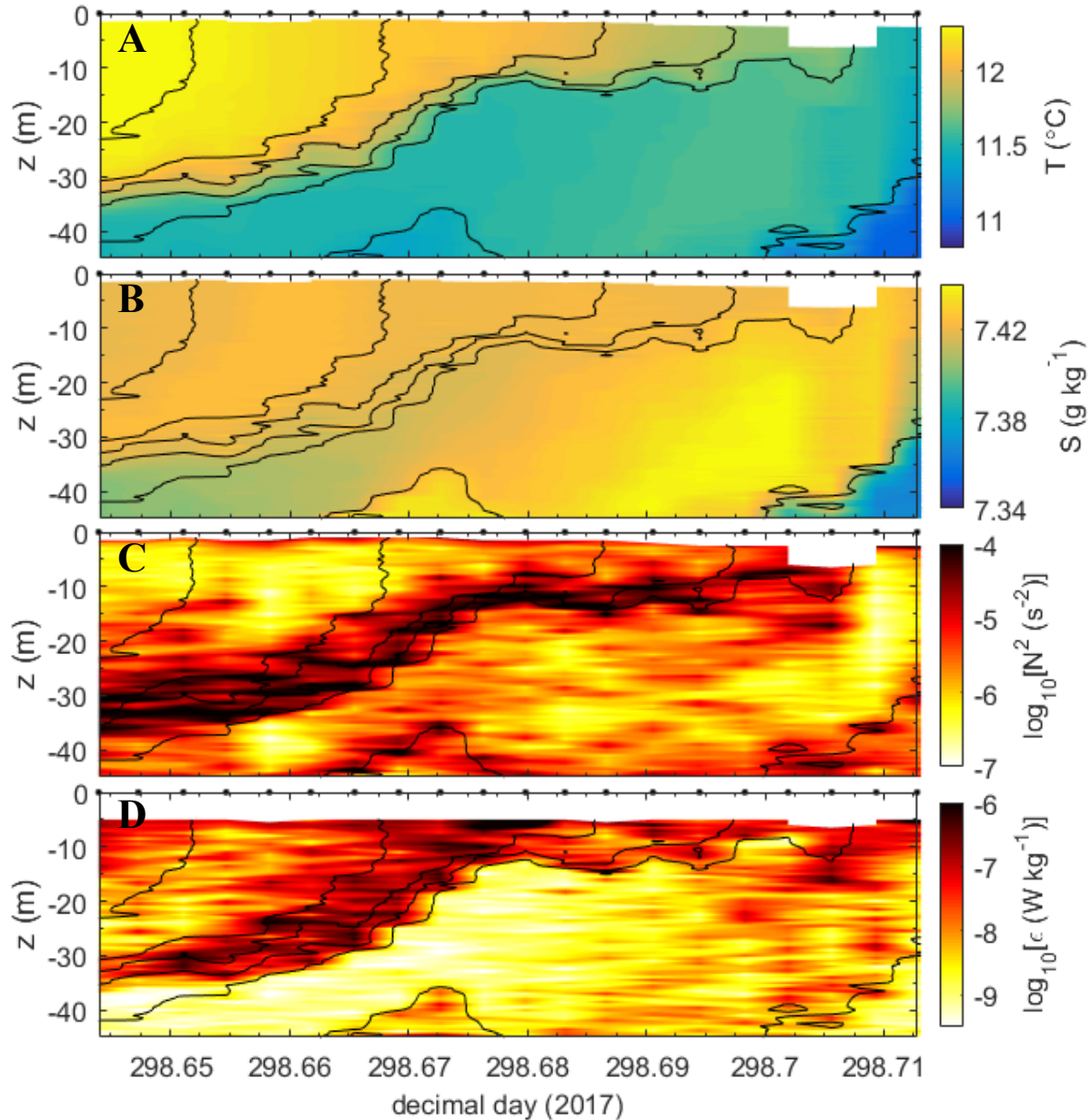


Figure 5.8: Enlarged plots of (A) conservative temperature, (B) absolute salinity, (C) buoyancy frequency squared and (D) dissipation rate of the second transect of period I, marked in a black rectangle in Fig. 5.6, describing the turbulent front. Black contour lines denote density isopycnals; notice that the density increments have been decreased compared to Fig. 5.6 to reveal the structure of the surface layer. Black bullet markers indicate individual MSS profiles.

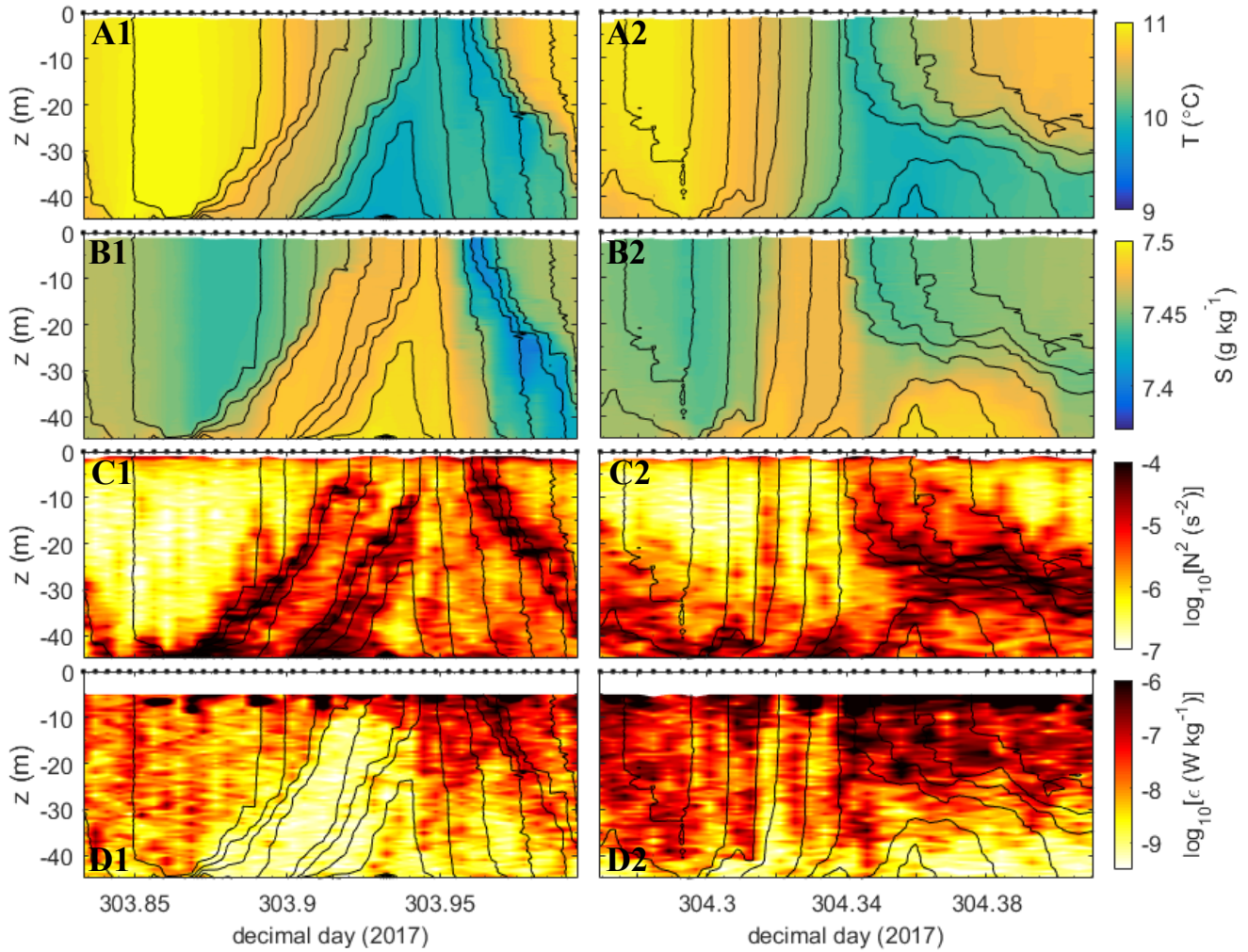


Figure 5.9: Enlarged plots of the (A1, A2) conservative temperature, (B1, B2) absolute salinity, (C1, C2) buoyancy frequency squared and (D1, D2) dissipation rate of the third and fifth transect, respectively, of period II, marked in black rectangles in Fig. 5.7, describing the turbulent filament. Black contour lines denote density isopycnals; notice that the density increments have been decreased compared to Fig. 5.7 to reveal the structure of the surface layer. Black bullet markers indicate individual MSS profiles.

# Chapter 6

## Summary

### 6.1 Summary

The main focus of this thesis was to examine some of the most important mixing processes of the Baltic Sea. First, the contribution of near-inertial waves to mixing in the surface and interior of the ocean was analyzed. This was followed by the study of lateral density gradients and their effects on the structure of the surface boundary layer. The investigation was based on hydrographic and turbulence measurements obtained in the Eastern Gotland Basin.

The high-pass filtered velocity data obtained from the moored ADCPs, revealed that the velocities in the internal wave band were dominated by clockwise rotating near-inertial motions, both in the surface and interior layers. However, stronger signals were observed in the halocline region. Depending on the tilt of the phase lines, it was suggested that these signals were either generated locally at the topographic slope close to the mooring, or resulted from the delayed arrival of higher internal wave modes generated at the lateral boundaries far from the mooring. In both cases, the observed out of phase motions above and below the halocline led to the generation of vertical shear layers that could potentially result to mixing. The dissipation measurements obtained from the microstructure profiler in the vicinity of station TRR1, indicated different turbulence regimes in the water column. Turbulence in the surface layer above the halocline was closely correlated to the wind forcing at the sea surface. On the other hand, turbulence in the interior of the water column, observed as patches of enhanced dissipation rates in and below the halocline, was quite independent of the surface forcing. These bands of turbulent dissipation, were likely energized by shear instabilities resulting from near-inertial motions.

The focus was then constrained to the surface boundary layer, in which observed lateral density gradients, associated with fronts and filaments, significantly modified its structure. This was revealed through two distinct cases. First, a case of a stratified while turbulent front was examined. It was found that turbulence developed within the front which was proposed to have resulted from the vertical shear driven by the density gradients during the geostrophic adjustment. Second, the case of a filament wedged between two fronts

was studied. It was found that during high winds, the filament appeared both stratified and turbulent. These observations led to the suggestion that strong winds simultaneously energized turbulence and submesoscale instabilities that acted to continuously restratify the surface layer.

## 6.2 Future Work

The bands of turbulent dissipation seen in the stratified interior are a major source of mixing inside the permanent halocline. Due to lack of time, it was only assumed that these bands have resulted from shear instabilities associated to near inertial motions. The computation of the vertical shear squared would suffice to prove this assumption. If the shear squared within the correlated bands exceeds the local value of the buoyancy frequency squared, then the gradient Richardson number could be close to the threshold for shear instability. However, the exact quantification of the gradient Richardson number is not that simple, as the shear and buoyancy frequency are measured at different vertical resolution and horizontal position. The subject of submesoscale instabilities, on the other hand, is more complicated. However, a starting point for future work could be to evaluate the direction of the wind relative to the direction of the frontal velocity.

# Appendix A

## Derivation of the Internal Gravity Wave Equation

The equation that governs the motions of internal gravity waves which is required to derive the dispersion relation, results from the combination of the following equations of motion (see Chapter 3.2):

$$\frac{\partial u}{\partial x} + \frac{\partial v}{\partial y} + \frac{\partial w}{\partial z} = 0, \quad (\text{A.1})$$

$$\frac{\partial u}{\partial t} - fv = -\frac{1}{\rho_0} \frac{\partial p'}{\partial x}, \quad (\text{A.2})$$

$$\frac{\partial v}{\partial t} + fu = -\frac{1}{\rho_0} \frac{\partial p'}{\partial y}, \quad (\text{A.3})$$

$$\frac{\partial w}{\partial t} = -\frac{1}{\rho_0} \frac{\partial p'}{\partial z} - \frac{\rho' g}{\rho_0}, \quad (\text{A.4})$$

$$\frac{\partial \rho'}{\partial t} - \frac{\rho_0 N^2}{g} w = 0, \quad (\text{A.5})$$

Following the analysis of Pedlosky (Pedlosky, 2013, p. 108), the first step is to take the curl of the horizontal momentum equations, i.e. subtract the  $x$ -derivative of the  $v$ -momentum equation (A.3) from the  $y$ -derivative of the  $u$ -momentum equation (A.2), and then invoke the continuity equation (A.1). Assuming the  $f$  plane approximation<sup>1</sup> is valid, one arrives to the relation,

$$\frac{\partial \zeta}{\partial t} = -f \left( \frac{\partial u}{\partial x} + \frac{\partial v}{\partial y} \right) = f \frac{\partial w}{\partial z} \quad (\text{A.6})$$

---

<sup>1</sup>In the  $f$ -plane approximation the Coriolis parameter  $f$  is assumed to be invariant with latitude.

where  $\zeta = \frac{\partial v}{\partial x} - \frac{\partial u}{\partial y}$  is defined as the relative vorticity. The next step is to take the divergence of the horizontal momentum equations, i.e. add the  $x$ -derivative of the  $u$ -momentum equation to the  $y$ -derivative of the  $v$ -momentum equation, to obtain

$$\frac{\partial^2 w}{\partial t \partial z} + f\zeta = \frac{1}{\rho_0} \left( \frac{\partial^2 p'}{\partial x^2} + \frac{\partial^2 p'}{\partial y^2} \right) = \frac{\nabla_H^2 p'}{\rho_0} \quad (\text{A.7})$$

where the definition of the relative vorticity and the continuity equation (A.1) were applied. Taking the time derivative of (A.7) and eliminating  $\zeta$ , yields an equation relating the horizontal divergence to the horizontal Laplacian of the pressure perturbation,

$$\left( \frac{\partial^2}{\partial t^2} + f^2 \right) \frac{\partial w}{\partial z} = \frac{1}{\rho_0} \frac{\partial}{\partial t} \nabla_H^2 p' \quad (\text{A.8})$$

Elimination of the density perturbation  $\rho'$  between the vertical momentum equation (A.4) and the density equation (A.5) gives

$$\frac{\partial^2 w}{\partial t^2} + N^2 w = -\frac{1}{\rho_0} \frac{\partial^2 p'}{\partial z \partial t} \quad (\text{A.9})$$

Finally, by taking the horizontal Laplacian of Eq. A.9 and combining the result with Eq. A.8, the pressure  $p'$  is eliminated and one arrives to the desired equation for the vertical velocity:

$$\boxed{\frac{\partial^2 (\nabla^2 w)}{\partial t^2} + N^2 \nabla_H^2 w + f^2 \frac{\partial^2 w}{\partial z^2} = 0} \quad (\text{A.10})$$

# Appendix B

## Digital Filters

Numerical filtering is an unavoidable step in the interpretation of oceanographic time series data, especially when one is interested in isolating phenomena with a certain frequency. Depending on the required analysis of the oceanographic records, low-pass, high-pass and band-pass filters can be applied, that leave, respectively, the low frequencies, the high frequencies or the frequencies within a central passband, unaffected (unity gain).

For the analysis of the ADCP timeseries data and the localization of near inertial waves, emphasis was given to the design and application of low-pass digital filters that attenuate frequencies well above the cut-off frequency (zero gain). One of the most suitable filters for the analysis of the ADCP data was thought to be the Butterworth filter, as it is both simple and effective. The gain of an  $n$ -order Butterworth lowpass filter is defined in terms of the square of its frequency response (or transfer function), as:

$$|W_B(\omega)|^2 = \frac{1}{1 + (\omega/\omega_c)^{2n}}, \quad (\text{B.1})$$

where  $\omega_c$  is the cut-off frequency and  $n$  is the order of the filter (Roberts and Roberts, 1978). The frequency response of a Butterworth filter is maximally flat (i.e. no ripples) in the pass-band and rolls off smoothly towards zero in the stop-band leaving the low frequency components unchanged (Roberts and Roberts, 1978). By increasing the order of the filter, the transition zone between the stop-band and the pass-band can be lowered so that unwanted high-frequency components are effectively removed. However, too sharp a transition zone might induce ringing effects in the output, known as Gibb's phenomenon, causing leakage of unwanted energy into the filtered record (Thomson and Emery, 2014, p.601). What is more, as the Butterworth filter is recursive, meaning that past output values contribute to future output values, a phase shift in the signal is generated (Roberts and Roberts, 1978). To ensure zero phase shift, the ADCP data has to be processed twice, first forwards and then backwards through the same filter. This zero-phase digital filtering doubles the order of the filter which was thought through when setting the filter order.

Another digital filter which was considered for the analysis of the ADCP time-series data, was the Boxcar averaging filter. The Boxcar averaging filter, the simplest form of

low-pass filters, moves through the data record, averaging connected subsets of the data, with equal weight given to each point in the subset.

A simple comparison between the two (see below), indicated that, in our case, the Butterworth filter is superior to the Boxcar. For this, a sinusoidal signal was considered of the form:

$$y = \sin\left(\frac{2\pi t}{T_f}\right), \quad (\text{B.2})$$

where  $T_f = \frac{2\pi}{f} = 14.26$  h, is the local inertial period at the location of the ADCP (57°08'N, 20°32'E). Observations are at discrete times,  $t = t_0 + n\Delta t$ ,  $n = 0, 1, \dots, 5 \times 10^3 - 1$  where  $t_0 = 1$  s denotes the start time of the record and  $\Delta t = 60$  s, the sampling period which coincides with the sampling period of the ADCP. The signal was then filtered for two separate cases: a) with a sixth-order low-pass Butterworth filter with a cut-off period varying from 15 h to 23 h (Fig. B.1) and b) with a Boxcar averaging filter with a window size also varying from 15 h to 23 h (Fig. B.2). From the Figures below, it can be seen that while in the Butterworth case the damping of the signal increases when increasing the cut-off period from 15 h to 23 h, in the Boxcar case, the damping of the signal behaves in a non-monotonic way. This is an important factor which renders the latter more effective for the analysis of the time-series data throughout this thesis.

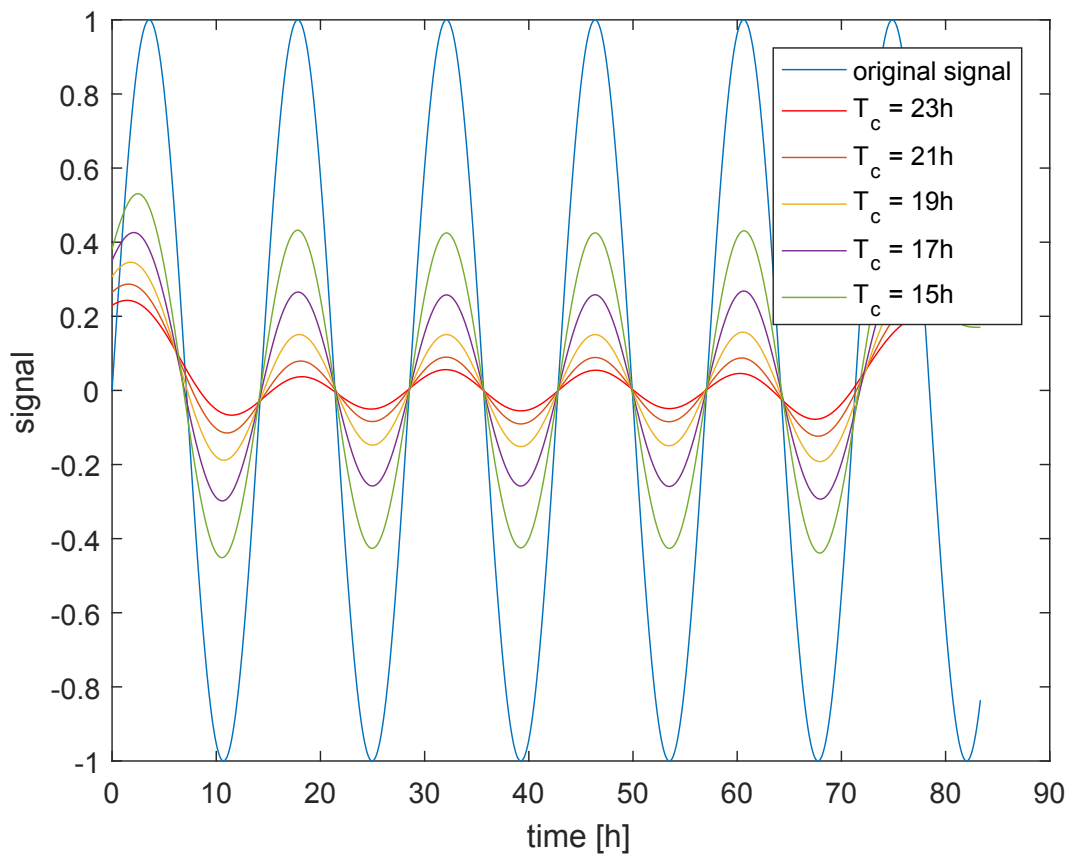


Figure B.1: Sinusoidal signal filtered with a sixth-order low-pass Butterworth filter. Notice how the damping of the signal increases when increasing the cut-off period from 15 h to 23 h.

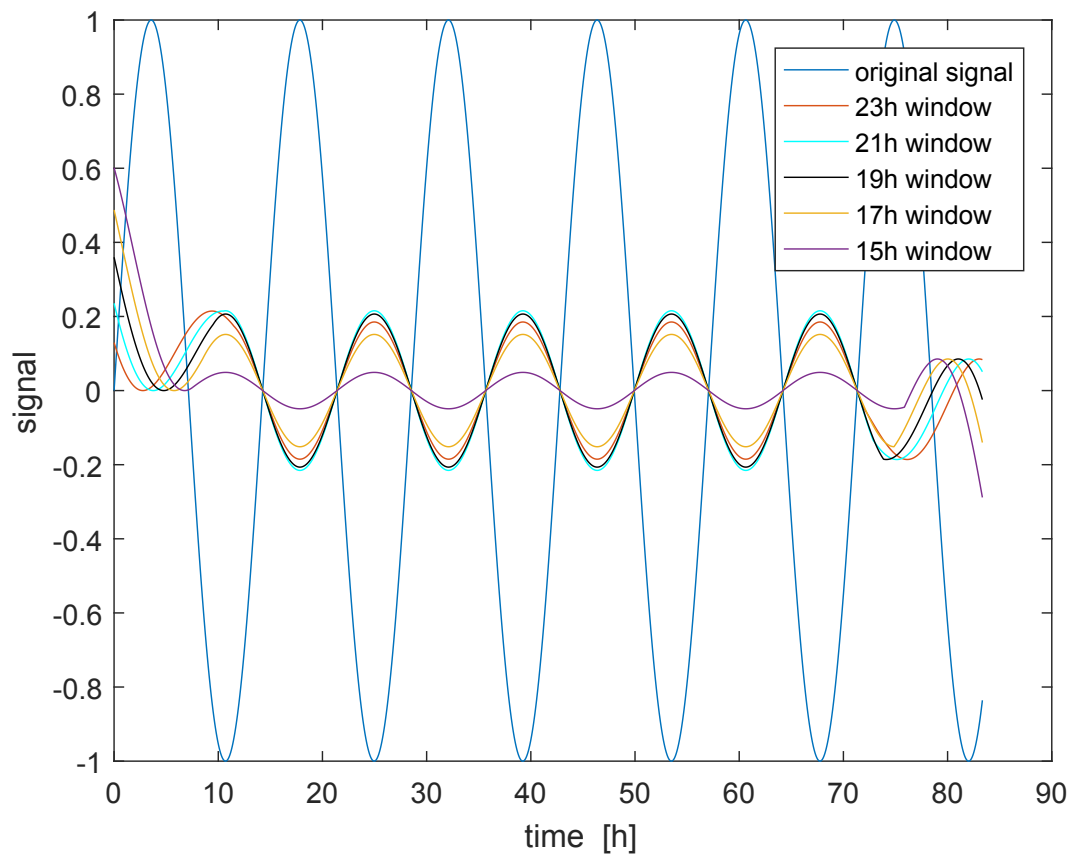


Figure B.2: Sinusoidal signal filtered with a Boxcar averaging filter. Notice how the damping of the signal behaves in a non-monotonic way.

# Bibliography

- Alford, M. H., MacKinnon, J. A., Simmons, H. L., and Nash, J. D. (2016). Near-inertial internal gravity waves in the ocean. *Annual review of marine science*, 8:95–123.
- Bergström, S. and Carlsson, B. (1994). River runoff to the Baltic Sea, 1950-1990. *Ambio*, 23(4-5):280–287.
- Boccaletti, G., Ferrari, R., and Fox-Kemper, B. (2007). Mixed layer instabilities and restratification. *Journal of Physical Oceanography*, 37(9):2228–2250.
- Eckart, C. (1948). An analysis of the stirring and mixing processes in compressible fluids. *J Mar Res*, 7(3):265–275.
- Ekman, V. W. (1905). *On the influence of the Earth's rotation on ocean-currents*.
- Feistel, R., Nausch, G., and Wasmund, N. (2008). *State and evolution of the Baltic Sea, 1952-2005: A detailed 50-year survey of meteorology and climate, physics, chemistry, biology, and marine environment*. John Wiley & Sons.
- Ferrari, R. (2011). A frontal challenge for climate models. *Science*, 332(6027):316–317.
- HELCOM (2002). Environment of the Baltic Sea area: 1994-1998. *Baltic Sea Environment Proceedings*, (82A).
- Holtermann, P. L., Umlauf, L., Tanhua, T., Schmale, O., Rehder, G., and Waniek, J. J. (2012). The Baltic Sea tracer release experiment: 1. Mixing rates. *Journal of Geophysical Research: Oceans*, 117(C1).
- IOC, S. et al. (2010). The international thermodynamic equation of seawater: Calculation and use of thermodynamic properties. Intergovernmental Oceanographic Commission, Manuals and Guides no. 56. In *Manual and Guides*, volume 56. UNESCO.
- Kolmogorov, A. N. (1941). The local structure of turbulence in incompressible viscous fluid for very large Reynolds numbers. In *Dokl. Akad. Nauk SSSR*, volume 30, pages 299–303.
- Köuts, T. and Omstedt, A. (1993). Deep water exchange in the Baltic Proper. *Tellus A: Dynamic Meteorology and Oceanography*, 45(4):311–324.

- Kundu, P. K. (1993). On internal waves generated by travelling wind. *Journal of Fluid Mechanics*, 254:529–559.
- Kundu, P. K., Chao, S.-Y., and McCreary, J. P. (1983). Transient coastal currents and inertio-gravity waves. *Deep Sea Research Part A. Oceanographic Research Papers*, 30(10):1059–1082.
- Kundu, P. K. and Cohen, I. (1990). *Fluid Mechanics*. Academic Press.
- Lappe, C. and Umlauf, L. (2016). Efficient boundary mixing due to near-inertial waves in a nontidal basin: Observations from the Baltic Sea. *Journal of Geophysical Research: Oceans*, 121(11):8287–8304.
- Lass, H. U., Prandke, H., and Liljebladh, B. (2003). Dissipation in the Baltic Proper during winter stratification. *Journal of Geophysical Research: Oceans*, 108(C6).
- Leppäranta, M. and Myrberg, K. (2009). *Topography and hydrography of the Baltic Sea*. Springer.
- Matthäus, W. and Franck, H. (1992). Characteristics of major Baltic inflows—a statistical analysis. *Continental Shelf Research*, 12(12):1375–1400.
- Olbers, D., Willebrand, J., and Eden, C. (2012). *Ocean Dynamics*. Springer Science & Business Media.
- Osborn, T. (1980). Estimates of the local rate of vertical diffusion from dissipation measurements. *Journal of Physical Oceanography*, 10(1):83–89.
- Pedlosky, J. (2013). *Waves in the ocean and atmosphere: Introduction to wave dynamics*. Springer Science & Business Media.
- Prandke, H. and Stips, A. (1998). Test measurements with an operational microstructure-turbulence profiler: Detection limit of dissipation rates. *Aquatic Sciences*, 60(3):191–209.
- Rak, D. and Wiczorek, P. (2012). Variability of temperature and salinity over the last decade in selected regions of the southern Baltic Sea. *Oceanologia*, 54(3):339–354.
- Reissmann, J. H., Burchard, H., Feistel, R., Hagen, E., Lass, H. U., Mohrholz, V., Nausch, G., Umlauf, L., and Wiczorek, G. (2009). Vertical mixing in the Baltic Sea and consequences for eutrophication—a review. *Progress in Oceanography*, 52(1):47–80.
- Reynolds, O. (1883). Xxix. An experimental investigation of the circumstances which determine whether the motion of water shall be direct or sinuous, and of the law of resistance in parallel channels. *Philosophical Transactions of the Royal Society of London*, 174:935–982.
- Roberts, J. and Roberts, T. D. (1978). Use of the butterworth low-pass filter for oceanographic data. *Journal of Geophysical Research: Oceans*, 83(C11):5510–5514.

- Rossby, C.-G. (1938). On the mutual adjustment of pressure and velocity distributions in certain simple current systems, ii. *J. mar. Res.*, 1(3):239–263.
- Smyth, W. D. and Moum, J. N. (2000). Length scales of turbulence in stably stratified mixing layers. *Physics of Fluids*, 12(6):1327–1342.
- Stewart, R. and Grant, H. L. (1962). Determination of the rate of dissipation of turbulent energy near the sea surface in the presence of waves. *Journal of Geophysical Research*, 67(8):3177–3180.
- Tandon, A. and Garrett, C. (1994). Mixed layer restratification due to a horizontal density gradient. *Journal of Physical Oceanography*, 24(6):1419–1424.
- Taylor, J. R. and Ferrari, R. (2010). Buoyancy and wind-driven convection at mixed layer density fronts. *Journal of Physical Oceanography*, 40(6):1222–1242.
- Thomson, R. E. and Emery, W. J. (2014). *Data analysis methods in physical oceanography*. Newnes.
- Thorpe, S. A. (2005). *The Turbulent Ocean*. Cambridge University Press.
- Van der Lee, E. and Umlauf, L. (2011). Internal wave mixing in the Baltic Sea: Near-inertial waves in the absence of tides. *Journal of Geophysical Research: Oceans*, 116(C10).
- Welander, P. (1955). Studies on the general development of motion in a two-dimensional, ideal fluid. *Tellus*, 7(2):141–156.
- Whitt, D. B. and Taylor, J. R. (2017). Energetic submesoscales maintain strong mixed layer stratification during an autumn storm. *Journal of Physical Oceanography*, 47(10):2419–2427.